University of Padova

Department of Information Engineering

Master Thesis in ICT for Internet and Multimedia - Telecommunications

Starlink Receiver Prototyping for Opportunistic Positioning

Supervisor
Nicola Laurenti
University of Padova

Master Candidate
Alessio Curzio

Student ID
2037848

Academic Year
2022-2023

Graduation date
October 12, 2023

Abstract

Traditional GNSS systems for positioning (PNT), such as GPS and Galileo, use Medium Earth Orbits (MEO). Recently, the possibility to use Low Earth Orbit (LEO) orbits for PNT has been investigated, which offer several advantages over the traditional MEO, e.g., higher power and wider band. Among the available signals of opportunity (SOOPs), this thesis project investigates the feasibility of utilizing Starlink signals, primarily designed for global Internet coverage, for positioning purposes. The Starlink signal structure is not publicly available, but the literature suggests the presence of nine equidistant spectral peaks within a band of approximately 1 MHz in the signal spectrum of each satellite, centered at frequency 11, 325 GHz. The method proposed in this thesis involves the acquisition and tracking of these peaks, on a signal sampled at a lower frequency than the estimated bandwidth for the entire Starlink channel of 240 MHz, in order to reduce receiver complexity. For the acquisition phase, once the IQ components have been extracted from the signal, the optimal acquisition window length is selected as the trade-off between noise and Fast Fourier Transform (FFT) computational performance. The peak detection threshold is chosen based on the Gaussian distribution of noise and a predefined false alarm probability. This enables the selection of peaks above the noise floor in each acquisition instance, facilitating the detection of potential satellites. Then, similar to standard GNSS receivers, a tracking loop (a third-order PLL assisted by a second-order FLL) is implemented to estimate the Doppler frequency shift of the peaks over the entire captured window. However, as opposed to standard GNSS signals, Starlink does not use a PRN code to identify the individual satellites. To resolve the ambiguity in satellite identification, a method is proposed to compare the Doppler frequency shifts estimated from peak tracking with the Doppler frequency shifts predicted by a visibility prediction tool, which provides the ability to associate each identified peak with a specific Starlink satellite. The tool uses Two-Line Element Sets (TLEs) data and a simplified perturbation model (SGP4) to propagate the satellite orbits. The method is applied to a signal captured using a basic configuration with a Ku-band Low Noise Block (LNB) converter, and the data acquired consist of raw In-phase and Quadrature-phase (IQ) samples with a bandwidth of 4,096 MHz around 11,325 GHz. The results show that the method allows to acquire several satellites in the captured signal, and to track the corresponding peaks for positioning purposes.

Contents

Listing of figures

Listing of tables

Listing of acronyms

CW . . . . . Continuous Wave
DSSS . . . . . Direct Sequence Spread Spectrum
EKF . . . . . Extended Kalman Filter
ESA . . . . . European Space Agency
FFT . . . . . Fast Fourier Transform
FLL . . . . . Frequency Locked Loop
GNSS . . . . . Global Navigation Satellite System
IMU . . . . . Inertial Measurement Unit
INS . . . . . Inertial Navigation System
IQ . . . . . In-phase and Quadrature components
KF . . . . . Kalman Filter
LEO . . . . . Low Earth Orbit
LNB . . . . . Low Noise Block
LO . . . . . Local Oscillator
LPF . . . . . Low-Pass Filter
MEO . . . . . Medium Earth Orbit
NCO . . . . . Numerically Controlled Oscillator
PLL . . . . . Phase Locked Loop
PNT . . . . . Positioning, Navigation, Timing
PRN . . . . . Pseudo-random noise
PSS . . . . . Primary Synchronization Signal
PVT . . . . . Position, Velocity, Time
QAM . . . . . Quadrature Amplitude Modulation
SDR . . . . . Software Defined Radios
SGP . . . . . Simplified General Perturbations
SNR . . . . . Signal-to-noise Ratio
SOOP . . . . . Signals of Opportunity
SS . . . . . Spread Spectrum

SSS . . . . . Secondary Synchronization Signal
SV . . . . . Space Vehicle
TLEs . . . . . Two-line Element Set

1 Introduction

Humans have always been motivated by the desire to accurately determine their position. This intrinsic need, deeply rooted in our evolution, has led generations of scientists to develop and perfect instruments capable of ensuring our correct orientation, whether at sea, in the air, or on land. The ability to accurately determine one's location is important: not only is it essential for navigation and reaching specific destinations, but it also plays a key role in territorial knowledge and mapping, infrastructure construction, and traffic management.

Although GPS was a major revolution in global positioning, it is not the only system available today. Other MEO (Medium Earth Orbit) satellite constellations, such as Galileo in Europe, GLONASS in Russia, and Beidou in China, have emerged, and more are under development. Combined, these systems form the Global Navigation Satellite System (GNSS). But geomatics, the science that studies these methods, is already looking to the future, envisioning new frontiers and possibilities, including the development of LEO (Low Earth Orbit) navigation systems.

1.1 Background and Motivation

These LEO satellites offer several advantages over traditional MEO satellites: they are closer to Earth, which means their signals can be more powerful and have a wider bandwidth. LEO signals also have security features that allow for quick two-way authentication checks [5]. This

could result in greater accuracy and reliability of the received signal. However, the true potential of LEO satellites for positioning has not yet been fully explored.

The recent development of the Starlink constellation, designed to provide global Internet coverage, has raised the question of whether these satellites can also be used for positioning. Although the signal structure of Starlink is not publicly available, clues from the literature suggest that there may be opportunities to explore in this area.
Furthermore, the use of Signals of Opportunity (SOOP) for navigation and positioning is not a new concept, but applying this idea to Starlink signals could open new frontiers in the field of positioning.

1.2 Objective of the Thesis

The main objective of this thesis is to investigate the feasibility of using Starlink signals for positioning. This includes analyzing the structure of the signal, proposing a method for acquiring and tracking these signals, and finally, practically verifying the condition of these signals to provide accurate position estimates.

A particular focus will be on reducing the complexity of the receiver by taking advantage of a lower sampling bandwidth than that estimated for the entire Starlink channel. This could make the technology more affordable and reduce associated costs. Another key aspect of this research will be to resolve the ambiguity in satellite identification due to the lack of a PRN code in Starlink signals. A method will be proposed to compare Doppler frequency estimates obtained from tracking with those predicted by a visibility prediction tool.

In summary, this thesis aims to provide a comprehensive review of the potential and challenges associated with the use of the Starlink constellation for positioning applications, and to provide new insight regarding how LEO signals can be used in this area in the future.

2

State Of Art

2.1 Signals for Navigation

Satellite navigation has its origins in the early experiments with artificial satellites during the Cold War in October 1957, in particular, with the launch of Sputnik 1 by the Soviet Union. Although Sputnik was designed primarily as a demonstration of technological capabilities and had no inherent navigational functions, scientists discovered an unexpected application: by monitoring the frequency of Sputnik's radio signal, it was possible to determine the satellite's position on Earth through the Doppler frequency shift of the signal as it moved.
This Sputnik signal phenomenon was used by scientists for the determination of the satellite's position and speed. A few years later, the United States introduced the Transit system, heralded as the first true satellite navigation system. Its primary application was to aid the navigation of U.S. Navy submarines. Like Sputnik, Transit was based on Doppler shift principles, using changes in signal frequency to infer receiver positions [6] [7].

Over time, these rudimentary systems have been significantly refined. They incorporate advanced technologies and algorithms to improve accuracy and reliability. In addition, the range of applications expanded beyond military navigation to include civil aviation, shipping, and even personal use.

2.1.1 Medium Earth Orbit Positioning, Navigation, and Timing

These early efforts set the path for today's GNSS, capable of offering global coverage and satisfying a wide range of civil and military applications. Systems like the GPS (U.S.), GLONASS (Russia), GaliLEO (Europe), and BeiDou (China) operate using satellites in MEO to provide precise positioning, navigation, and timing capabilities [8]. The range of these orbits is from 2.000 to about 35.000 km altitude.

While early satellite navigation systems like Transit relied on Doppler shift principles, modern GNSS systems like GPS and Galileo use a more sophisticated approach. Their signals are generated using the well-known Direct Sequence Spread Spectrum (DSSS) technique. DSSS represents a specific case of the Spread Spectrum (SS) approach. They perform the spreading and dispreading operation by means of a Pseudo Random Noise (PRN) code attached to the communication channel [9]. This provides greater resistance to interference and improves the accuracy of the measurements. These advancements represent a considerable leap in both technology and capability, providing a more robust and precise system.

The utilization of MEO for GNSS became the standard for many years due to its balance of coverage and signal accuracy.

2.1.2 Low Earth Orbit Positioning, Navigation, and Timing

As reliance on the GNSS continues to grow, so does the range of threats - both natural and man-made - that could degrade or deny it. This is driving the need to explore new technologies for navigation and timing [10].

As a result, the use of LEO, whose satellites operate at an altitude of up to 2.000 kilometers, has been explored.

The idea of using LEO for positioning, navigation and timing (PNT) functions has gathered support due to several inherent advantages. For example, satellites in LEO orbits are closer to Earth, which can result in lower latency and potentially higher data rates. The reduced distance also allows for lower power ground-based receivers, making the technology more accessible and cost-effective.

This uptrend, that has seen a significant acceleration over the past few years, is based on a dual foundation: the promise of powerful satellite navigation systems that address emerging user needs, such as autonomous navigation technologies, and the attraction of economically sustainable constellations. This latter opportunity owes its origin to the advent of redefined industrial and business frameworks for LEO, commonly denominated as "New Space" [11] [12].

Designing a LEO satellite constellation involves selecting orbit configurations, establishing ground infrastructure, and considering the number of ground stations required for satellite communication. High inclination orbits are preferred in LEO to expand coverage in high latitude areas.

LEO-PNT systems can be divided in three categories of concepts according to the way the signals are designed and featured [1]:

1. **Dedicated LEO Signals:** Novel LEO-PNT systems with optimised design parameters for positioning and navigation targets.
2. **LEO Signals of Opportunity:** No specific position signals are transmitted. In this case, the PNT computation is performed exclusively by the receiver. This eliminates the need for dedicated infrastructure, resulting in cost savings and faster implementation.
3. **LEO Signals aiding GNSS:** Use LEO satellites for signal aid, correction and back-up of conventional GNSS MEO satellites.

2.1.3 Low Earth Orbit vs Medium Earth Orbit

While MEO orbits begin at about 2.000 km above sea level and can extend to about 35.000 km, it is interesting to note that satellite navigation systems operating in MEO are always at least 19.100 km from Earth. This considerable distance causes signal attenuation due to the inevitable losses that occur as the signal travels through space between the satellite and the Earth [1]. On the other hand, LEO signals experience more favourable link budget compared to GNSS signals. As a function of the satellites operating at significantly different altitudes, a LEO signal received on the surface of the Earth can be up to 1000 times (30 decibels [dB]) stronger with respect to a MEO satellite as the antenna of the LEO satellites usually have broader field of view compared to GNSS ones [13]. The stronger signal means that LEO signals may have better penetration through obstructions and may be able to reach difficult or denied environments, such as deep urban areas or even indoors, which, along with the new geometries enabled by LEO satellites, should improve overall service availability and resilience [11].
LEO-PNT enables faster position fixes, facilitates rapid two-way authentication checks, and significantly improves signal availability, especially in high-latitude and polar regions [5]. Another aspect to consider is the difference in orbital period between MEO and LEO satellites. MEO satellites orbit the Earth twice a day, while LEO satellites have orbital periods of less than 128 minutes, allowing them to orbit the Earth more than 11 times a day. This difference in orbital period results in MEO satellites being visible for extended periods of time, often several hours,

while LEO satellites are only visible for brief intervals, typically less than 15 minutes. This results in a larger Doppler shift, which is easier to detect and measure for various applications such as precise tracking and navigation [14].

2.1.4 Dedicated LEO Signals

A dedicated LEO PNT system contains navigation parameters that are embedded in the RF signal, and the receiver is responsible for the decoding of the navigation messages. Dedicated LEO PNT systems do not yet exist globally, but there are efforts in this direction. An example of a company that is leading the PNT with a dedicated LEO service is Xona Space System [15]. They are planning to use this to their advantage and develop a LEO-PNT service, called Xona Pulsar, for the high-reliability sector of autonomous vehicles.
A practical strategy for developing a LEO-PNT system might be to emulate the design principles of existing GNSS signals, taking advantage of the rich expertise in this area. Specifically, a dedicated signal could operate on at least two frequencies (for ionospheric correction) and also with advanced error correction algorithms for increased robustness. This signal would traditionally have three core layers: the carrier wave, code and data modulations [1].

Three factors contribute to the increased accuracy gain of a dedicated LEO PNT signal over a carrier-based positioning system [1]:

1. **Code Gain:** It refers to the specific carrier wave modulation used to identify the transmitting satellite. A local replica of this signal is generated in the receiver on the user's end to facilitate correlation between the transmitted and received signals. The correlation process enables the acquisition and tracking of weaker signals, thereby enhancing pseudorange measurement capabilities in low-signal conditions.
2. **Transmitted Data:** They represent the information carried by the signal. In GNSS systems, this information typically consists of the navigation message or ephemeris. A LEO PNT system would also need to carry similar navigation information for precise positioning, adapted to the specific conditions of the LEO orbital environment.
3. **Timing Reference:** Accurate pseudorange measurements require high quality timing and frequency data. While GNSS satellites are equipped with highly precise and costly atomic clocks for this purpose, alternative timing references may be required for a LEO PNT system that is intended to operate independently of GNSS systems.

2.1.5 LEO Opportunistic Signals

SOOPs include a variety of RF signals not originally designed for navigation, such as those from communications systems, cellular and satellite networks, televisions, AM/FM radios, and radar systems.
The advantages of using SOOP for navigation include the free availability of existing infrastructure, higher signal power compared to GNSS signals, and a wide range of frequencies if multiple systems are used. However, there are drawbacks. SOOP signals are not designed for navigation, leading to potential problems such as inconsistent availability, lack of synchronization between different transmitters, and lower clock stability compared to GNSS satellites. In addition, the locations of the transmitters are not known. If one chooses to integrate different systems, the requirements include multi-band antennas, a multi-band RF front-end, and adequate computing resources [10]. In a LEO-PNT context, frequency conversion may be necessary when operating on K-band frequencies (such as Ku, K, Ka). Refer to the table 2.2 for details on the frequency ranges used.

The key differences between LEO-PNT and GNSS are the positioning structure, the navigation parameter assumptions, and the design of the signal acquisition and tracking loops. Unlike GNSS systems, a SOOP does not provide a coded signal to be replicated and compared within a user receiver, thus eliminating the need for correlators. This implies the absence of ephemeris, which are decoded in the message in the case of dedicated positioning systems.
The potential strength of K-band frequencies is evident when considering transmissions from mega-constellations in LEO orbit. Because of their large number of satellites, these constellations can provide consistent signal coverage worldwide. To take full advantage of these signals, a receiver may need additional down-conversion in its radio front-end, a topic discussed in more detail in later chapters.

2.1.6 Doppler Shift-Based Positioning

In navigation systems, a specialized filter is used to obtain the final position estimate. Among these, the Extended Kalman Filter (EKF) is a commonly used filter, although alternative methods are also applied. To refine these estimates, it's critical to identify and compensate for any gaps in the navigation data. This fine-tuning involves adjusting the way signals are acquired and tracked, and may also include additional metrics such as elevation [1]. When it comes to Doppler-based position tracking, either a phase-locked loop approach (PLL) is often used or a Kalman filter-based (KF) method is implemented, as shown in [16] and [2].

In Doppler-based positioning, the lack of ephemeris information typically results in the use of publicly available Two-Line Element Sets (TLEs) files to update both the navigation system and the satellite receiver [17]. Although the vertical accuracy of Doppler measurements is inferior, it can be improved by integrating altimeters. It is also common to add other instruments, such as an Inertial Measurement Unit (IMU) or Inertial Navigation System (INS), to provide more accurate measurements of the velocity of a moving receiver. [2]. To simplify the analysis, errors due to the ionosphere and troposphere are usually omitted.
In Doppler-based positioning systems, the accuracy of the clock in the receiver plays a critical role. As shown in [18], it's possible to achieve timing accuracy in the millisecond range.
To take advantage of signals from different satellite constellations, it may be advantageous to have multiple independent channels, which would require the use of multiple radio front-ends for the user. The bandwidth required for these operations is also closely related to the specific frequencies of the incoming signals. For LEO signals, the Doppler frequency shift can change dramatically during a single overhead pass, requiring sampling over a wide range of bandwidths [1].

A review of Doppler LEO PNT receiver configurations and their respective user location performance is presented in Table 2.1. A customized Software-Defined Radio (SDR) methodology is a common feature of all these configurations. The accuracy of the simulated models exceeds that of the real-world implementations, largely due to the assumptions of having access to more satellites and more accurate information about their status. Preliminary tests with multiple Starlink satellites indicate a general shift toward improved accuracy.
The most accurate user location performance, achieving about 7,7 meters of accuracy, uses six Starlink satellites, an altimeter, and a dedicated SDR system, as shown in [2].

2.2 LEO Constellations and Signals

2.2.1 Constellations, Bands and Usages

Information on frequency band classifications, their range, common applications, representative constellations, and the orbits where these signals are prevalent is summarized in Table 2.2. Figure 2.1 visualizes the characteristics of these frequency bands, focusing on elements such as antenna dimensions, bandwidth, data rates, susceptibility to atmospheric degradation, and general usage. The figure illustrates the inherent trade-offs between these attributes [1].

For example, although the use of higher carrier frequencies allows for greater theoretical data

Receiver Configuration	User Velocity	Constellation	Measurement	Estimator	Accuracy [m]	Ref.
Equipped with an altimeter	Static	Orbcomm	Pseudorange rate	EKF	11.38 (2D, simulated), 358 (2D, experimental), (both including height info.)	[17]
Equipped with INS	Dynamic	Globalstar, Orbcomm, Iridium, Starlink	Pseudorange rate	EKF	10.5 (simulated GOI), 10.1 (simulated Starlink)	[19]
Equipped with INS	Dynamic	Orbcomm	Pseudorange rate	EKF	416.5 (experimental)	[19]
KF-loops in SDR	Static	Starlink	Carrier phase	Least Square	7.7 including height info. (2D), 25.9 without height info. (2D), 33.5 without height info. (2D) (all experimental)	[2]
Multi-constellation switching mode	Static	Iridium,Orbcomm	Pseudorange rate	EKF	177.1 (3D, experimental), 132 (2D, experimental)	[16]
Quadratic square accumulating Doppler Shift	Static	Iridium	Doppler-shift	Least Square	400 (3D, experimental), 163/198 including height info. (2D, experimental)	[20]
Equipped with INS	Dynamic	Iridium	Pseudorange and range rate	KF	200 m to 1 km (simulated)	[21]
Mobile receiver and base station	Dynamic	Orbcomm, Iridium, Starlink	Differential Doppler measurement with AOA	KF	100 m within 2 km of base station (simulated)	[22]

Table 2.1: Overview of user receiver accuracy in Doppler positioning [1].

throughput due to the enhanced capabilities of multi-antenna arrays, it also comes with drawbacks such as increased atmospheric interference and reduced effective range. As shown in Figure 2.1, there is no one-size-fits-all frequency band for specific LEO satellite applications. The final decision should also take into account regulatory compliance and the financial considerations associated with antenna design [1].

LEO systems predominantly use the Ku and Ka frequency bands. However, emerging systems are gradually migrating to the higher frequency Q/V bands [1].

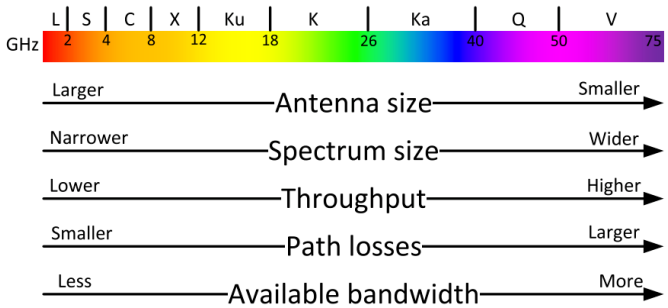

Figure 2.1: Frequency bands in terms of antenna size, spectrum size, throughput, path loss, and available bandwidth [1].

2.2.2 Starlink Downlink Signal Structure

Among the available SOOPs, this thesis project investigates the feasibility of utilizing Starlink signals, primarily designed for global internet coverage, for positioning purposes.

Frequency Band	Frequency	Typical Usage	Constellation Examples	Orbits
UFH	0.3 – 3 GHz	IoT	Myriota; Hiber	LEO
L-Band	1 – 2 GHz	PNT; Communications	GPS; Galileo; Iridium	MEO; LEO
S-Band	2 – 4 GHz	Communications; Earth observation	Inmarsat; Helios Wire	GEO; LEO
C-Band	4 – 8 GHz	Communications; Satellite TV	Eutelsat; Telesat	LEO
X-Band	8 – 12 GHz	Military; Weather monitoring	BlackSky Global	LEO
Ku-Band	12 – 18 GHz	Communications; TV; Broadband services	OneWeb; Starlink	LEO
K-Band	18 – 26 GHz	Short-range applications	N/A	N/A
Ka-Band	26.5 – 40 GHz	TV; Broadband services	Starlink; Kuiper; Teledesic; Viasat	LEO; GEO
Q-Band	33 – 50 GHz	Communications; Radio astronomy; Gateway links	Jupiter-3; BlueWalker-3	LEO
V-Band	40 – 75 GHz	Communication; Broadband services	OneWeb; Starlink	LEO

Table 2.2: Typical use of satellite constellation frequency bands [1].

Although Starlink's signal structure is not publicly available, recently information on Starlink's downlink signal structure has been estimated and published in [23]. On this publication, it has been estimated an OFDM model for Starlink signals due to its spectrally flat frequency block. In the frequency domain, as shown in Figure 2.2b, a total of eight channels, each with a bandwidth of F_s = 240 MHz, span the band allocated for Starlink's Ku-band downlink. It was assumed that neighboring cells would be served with different channels to avoid inter-cell interference. The two lower channels, centered at F_{c1} and F_{c2}, are currently unused. The middle four subcarriers of each channel are vacant, leaving a mid-channel gutter. Reserving such a gutter is a common practice in OFDM; otherwise, leakage from a receiver's mixing frequency may corrupt the central information symbols. In the case of Starlink, a transmitter-side leakage tone is present in some gutters for some satellites.

A guard band with a generous bandwidth of $F_g = 10$ MHz separates adjacent channels. Within some guard bands there appears a comb of 9 leakage tones uniformly spaced over a bandwidth of approximately 350 kHz [23].

Regarding the time domain layout, as shown in Figure 2.2b, each frame consists of 302 intervals of length $T_{sym} = 4.4$ µs plus a frame guard interval T_{fg}, for a total frame period of $T_f = 1/750$ s. Each frame begins with the Primary Synchronization Sequence (PSS), which is natively represented in the time domain, followed by the Secondary Synchronization Sequence (SSS), which is formatted as a standard 4QAM OFDM symbol. Each frame ends with the CM1SS followed by the CSS and the frame guard interval. A subsequent frame may be immediately present or not, depending on user demand. The known information symbols of the SSS and CSS allow a receiver to perform channel estimation across all subcarriers at the beginning and end of each frame, permitting within-frame interpolation.

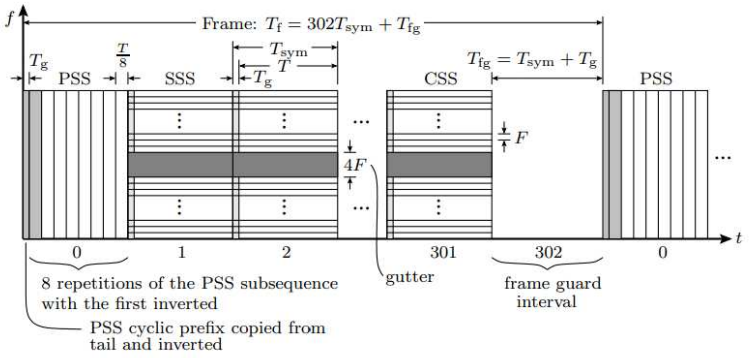

(a) Starlink Downlink Time Structure

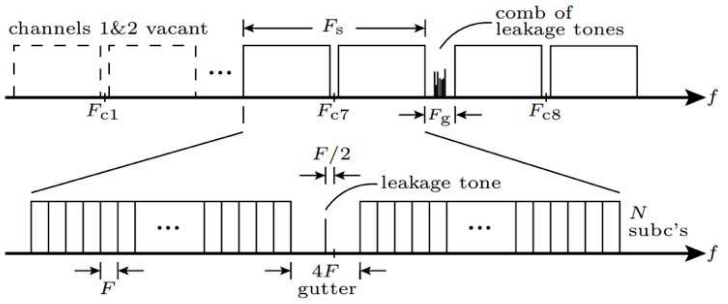

(b) Starlink Downlink Frequency Structure

Figure 2.2: Layout for the Ku-band Starlink downlink in time (a) and frequency (b).

2.2.3 Starlink Unmodulated Tones

The between-channel comb of tones shown in Figure 2.2b and described in the previous section are assumed to be the tones tracked in [2] to perform Doppler-based positioning with Starlink. It was noticed that these tones, when present, persist between frames and do not appear deliberately: their presence and amplitudes are not consistent from satellite to satellite, and appear to vary in amplitude with beam adjustments. The 9 peaks within some guard bands that can be acquired for each satellite are shown in Figure 2.3. The peaks appear to be uniformly spaced by about 44 kHz, and it was observed that the relative amplitudes of these nine peaks vary from one SV to another.

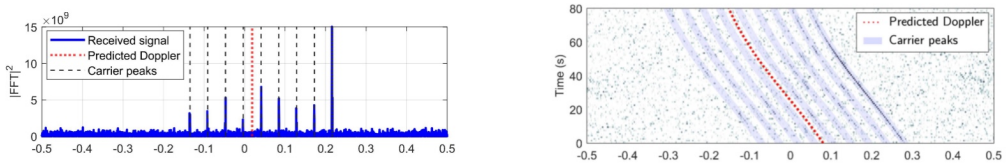

(a) Snapshot of the square of the FFT of the received signal along with the Doppler frequency predicted using TLEs

(b) Waterfall plot of the FFT of the received signal showing the nine peaks varying as the predicted Doppler

Figure 2.3: Example of the comb of tones in a Starlink downlink signal centered at frequency 11,325 GHz [2].

2.2.4 Use of Starlink Signals for Navigation

In the literature, two methods have been exploited to obtain positioning parameters from Starlink signals:

- The first method [23] is based on the OFDM structure of the signal (Wideband Spectrum). The main OFDM parameters have been estimated, including the PSS and SSS. By correlating the received signal with a local replica of the PSS and SSS, it is possible to estimate the delay for positioning purposes.
- The second method [2] consists of performing positioning based on tracking visible unmodulated tones present in a specific portion of the Starlink spectrum (Narrowband Spectrum).

The Table 2.3 shows the limiting ranges of the Starlink constellation in LEO orbit.

Name	Unit	A Typical Range Limit
Range	km	400 to 1150
Doppler Shift	kHz	-230 to 230
Doppler Shift Rate	kHz/s	< 5
Rate of the Doppler shift rate	Hz/s^2	< 70
Number of satellites in view	-	$16 - 35$
Satellite visibility time	minutes	< 4

Table 2.3: Typical range limits of LEO Starlink satellite [3].

2.3 Public Ephemerides and Propagation Models

2.3.1 Two-Line Element Sets (TLEs)

As noted in Section 2.1.6, when dealing with Doppler-based positioning with a SOOP, there is no navigation message to decode, and thus no ephemerides. TLE files, published by the North American Aerospace Defense Command (NORAD), are often used to fill this gap. They contain almanacs, i.e. data on the orbital state of the satellites, which are valid for 24 hours, but not very accurate.
These files provide details about an object's orbit around Earth at a particular time, also known as an epoch. When coupled with a propagation model, TLE data can be used to predict the position and velocity of a satellite at any given time. However, the error in position data can be several kilometers and tends to increase as time moves away from the epoch.
TLE correspond to the so-called NORAD format, the configuration of which is illustrated by the following example of an Starlink-1007 TLE:

```
STARLINK-1007
1 44713U 19074A   23247.54648211  .00010237  00000+0  70537-3 0  9996
2 44713  53.0548 343.8382 0002167  92.2444 267.8793 15.06389148210514
```

Lines 1 and 2 are the standard TLEs format identical to that used by NORAD and NASA. The format description is shown in Table 2.3.1 below [4]:

Line	Column	Description
1	01	Line Number of Element Data
	03-07	Satellite Number
	08	Classification (U=Unclassified)
	10-11	International Designator (Last two digits of launch year)
	12-14	International Designator (Launch number of the year)
	15-17	International Designator (Piece of the launch)
	19-20	Epoch Year (Last two digits of year)
	21-32	Epoch (Day of the year and fractional portion of the day)
	34-43	First Time Derivative of the Mean Motion
	45-52	Second Time Derivative of Mean Motion (Leading decimal point assumed)
	54-61	BSTAR drag term (Leading decimal point assumed)
	63	Ephemeris type
	65-68	Element number
	69	Checksum (Modulo 10)
2	01	Line Number of Element Data
	03-07	Satellite Number
	09-16	Inclination [Degrees]
	18-25	Right Ascension of the Ascending Node [Degrees]
	27-33	Eccentricity (Leading decimal point assumed)
	35-42	Argument of Perigee [Degrees]
	44-51	Mean Anomaly [Degrees]
	53-63	Mean Motion [Revs per day]
	64-68	Revolution number at epoch [Revs]
	69	Checksum (Modulo 10)

Table 2.4: The format description of Two-Line Element Set [4].

2.3.2 Simplified Perturbations Models - SGP4

The Simplified perturbations models, commonly known as SGP4, are a set of five mathematical models (SGP, SGP4, SDP4, SGP8, SDP8) used for calculating the orbital state vectors of satellites and space debris relative to Earth. Developed initially by Ken Cranford in 1970 and later refined, these models account for various perturbations such as Earth's shape, gravitational effects, drag, and radiation. SGP models focus on near-Earth objects with an orbital period under 225 minutes, while SDP models cater to objects with an orbital period above 225 minutes. These models are often used in conjunction with TLEs from NORAD and NASA for orbital prediction. The SGP4 model has an error of about 1 km at epoch, growing by 1-3 km per day. Over the years, revisions and improvements have been incorporated, to enhance their applicability for different space missions [24] [25].

3
Proposed Methods

In this chapter, the three basic phases that form the core of this thesis project are explored in detail: Acquisition, Tracking, and Visibility Predictor. These phases are shown schematically in the block diagram in Figure 3.1. The diagram is divided into two distinct branches, each with specific tasks.

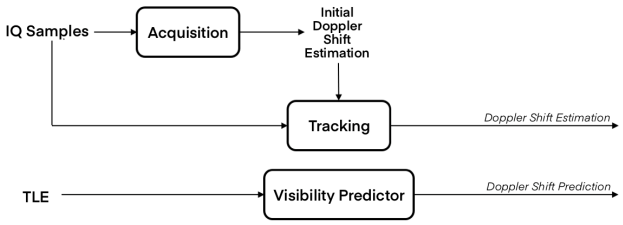

Figure 3.1: Block diagram of Acquisition, Tracking and Visibility Predictor phases.

The first branch starts with the IQ samples and proceeds through the acquisition and tracking phases. In this sequence, the IQ samples are first processed to acquire a signal from a specific satellite. Once acquired, the signal enters the tracking phase where frequency estimates are refined to ensure accurate and stable tracking of the satellite over time.

The second branch is independent of the first and begins with TLE files. These files feed the Visibility Predictor block, which uses the SGP4 model to calculate the predicted Doppler frequency shift. This step is particularly important when positioning using opportunistic signals, as in the case of Starlink. Unlike traditional satellite positioning systems that use ephemerides, opportunistic signals use TLE files and the Visibility Predictor to provide reliable predictions of satellite position and velocity.

3.1 Acquisition

In satellite positioning, signal acquisition is the initial phase that allows a receiver to lock onto a satellite's signal for subsequent localization and data decoding. In essence, acquisition is the process of identifying the specific time, frequency and phase at which a satellite transmits its signal. This is critical to establishing a link between the satellite and the receiver upon which subsequent operations such as tracking, positioning, and timing are based.

In the specific context of this thesis, the acquisition phase takes a unique form due to the characteristics of the Starlink signals. Unlike traditional GNSS, which transmit modulated signals specifically for positioning, from the Starlink systems it is possible to take advantage of unmodulated tones present within a certain frequency range, as described in section 2.2.3. As a result, conventional GNSS acquisition techniques are not directly applicable.

The custom Matlab tool developed for this thesis addresses this problem by employing specialized algorithms that can capture these unmodulated tones. Figure 3.2 shows the block diagram of the acquisition phase developed.

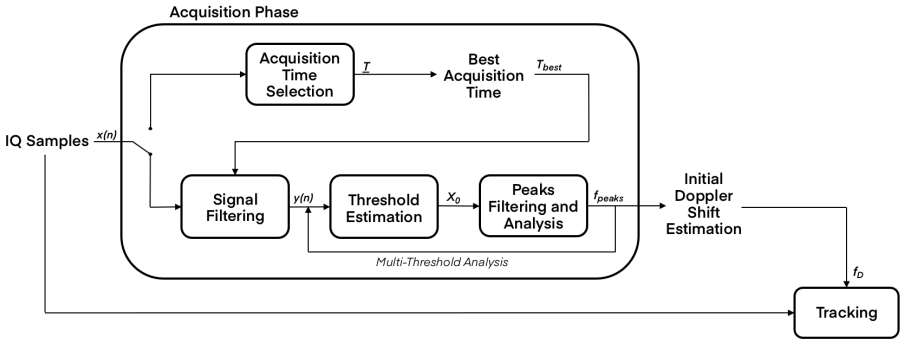

Figure 3.2: Block diagram of the Acquisition phase.

3.1.1 Estimation of Acquisition Window Length

There are several reasons for choosing an optimal acquisition window length for implementing the Fast Fourier Transform (FFT). Among them:

- First, the choice directly affects the computational complexity: a shorter acquisition window length results in a smaller FFT size, making it easier for the hardware to process.
- Second, the length of the acquisition interval can help control the effect of noise in the signal. A longer interval is often advantageous to significantly increase the signal-to-noise ratio.
- Finally, it is important to note that a longer acquisition window length can increase the phenomenon of *spectral leakage*, an effect that causes the energy of the signal to leak into adjacent bins of the FFT.

Within this thesis project, the approach to determine the optimal acquisition window length has been refined, based on the reformulation of the analysis presented in [3]. In order to identify an appropriate dimension for the FFT, an analysis was performed to determine the relationship between the maximum peak of the tone spectrum and the detection threshold as a function of a range of acquisition window lengths. As will be shown in chapter 4 with experimental results, this analysis will lead to the choice of the optimal window lengths T_{best}, as shown in the Figure 3.2. The threshold X_0 was calculated as shown in Section 3.1.3.

3.1.2 Signal Filtering

The signal of interest is complex IQ components in the time domain. Once imported into the Matlab environment and the acquisition window lengths estimated, the first key step is to apply advanced filtering and signal processing techniques. This step is critical to remove any distortion or noise from the signal, thereby facilitating and optimizing the initial acquisition phase.

Fix LNB initial accuracy

In the signal capture phase, a LNB was used to amplify and transmit the signal to the processing system. It is important to note that this device has an initial accuracy of up to a few MHz, depending on the technical specifications. This can result in a frequency shift that may introduce non-negligible errors in the subsequent analysis, thus compromising the quality and accuracy of the received signal.

To overcome this problem, the first fundamental step in our digital processing flow is to apply

a frequency shift to the signal. This correction is performed to precisely align the signal to the desired frequency, thereby compensating for inaccuracies introduced by the LNB.
Considering the complex signal IQ in the time domain $x(n)$, the frequency corrected signal is represented as:

$$x'(n) = e^{-j2\pi \widetilde{f} n T_s} \cdot x(n) \tag{3.1}$$

where T_S is the sampling period and $\widetilde{f}$ is the frequency error due to the initial accuracy of the LNB.

Spectral Leakage and Windowing

Accurate representation of signals in the frequency domain is a major concern in digital signal processing. When a finite portion of a signal is analyzed using the FFT, spectral leakage becomes a relevant issue. This phenomenon occurs when the energy of a frequency component is spread out in other frequency bins, creating a scattered appearance in the frequency spectrum.

To mitigate this problem, a *Windowing* method is used. The purpose of this practice is to modulating the signal in the time domain with a function that has an amplitude that smoothly decays to zero at its extremes. This makes it easier to join the beginning and end points of the waveform, resulting in a smoother signal without sudden jumps. This technique can be implemented using different types of window functions, each with specific frequency characteristics. A detailed analysis of the frequency characteristics of a window reveals a continuous spectrum consisting of a central lobe and numerous secondary or side lobes. This central lobe is aligned with each frequency component of the signal in the time domain, while the side lobes gradually attenuate toward zero. The size of these side lobes is an indicator of the effect of the windowing method on the frequencies adjacent to the central lobe. In general, reducing the height of the side lobes helps to minimize the dispersion in the computed FFT, although this may result in an increase in the bandwidth of the main lobe. The asymptotic decay of the side lobes, known as the side lobe roll-off rate, can be increased to further reduce the dispersion in the frequency domain [26].

In our case, a Hanning (Hann) window will be applied to our Starlink signal, which contains unmodulated tones. The Hann window is particularly favored for its smoothness, which leads to fewer and lower side lobes in the frequency response. Compared to the other windows, the Hann window gave the best results, isolating the peak most effectively and significantly reducing the side lobes. This will help in the process of analyzing and identifying the tones and thus the satellites.The Hann window in time and frequency domain is shown in Figure 3.3.

The mathematical expression for applying a Hann window $w(n)$ to a signal $x'(n)$ is:

$$x'_{\text{win}}(n) = w(n) \cdot x'(n) \tag{3.2}$$

Where $w(n)$ for a Hann window is defined as:

$$w(n) = 0.5 \left(1 - \cos\left(2\pi \frac{n}{N}\right)\right) \tag{3.3}$$

Here, n is the sample index and N is the total number of samples in the window.

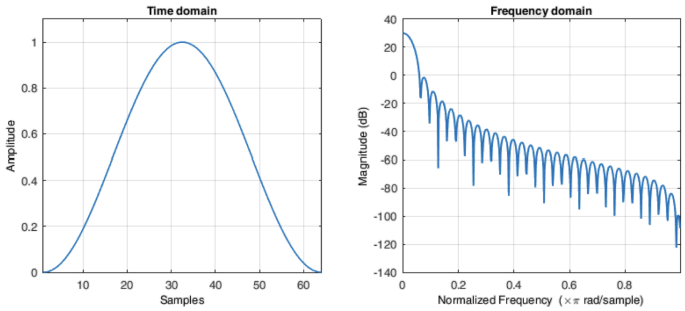

Figure 3.3: Hanning window in time and frequency.

Butterworth Filter

Considering the 9 individual tones for each satellite and a spacing of 44 kHz between each tone, the total signal occupies an approximate bandwidth of 400 kHz. Additionally, considering the maximum Doppler frequency shift that can occur in a LEO context, and including a portion of the spectrum with no tones for threshold estimation, it was chosen to configure the bandwidth of the Butterworth filter at 2 MHz. This choice was made to ensure effective signal cleanup.

The filter was designed to have specific passband and stopband characteristics, referring to the filter design scheme shown in Figure 3.4a. It was defined by the following parameters:

- $A_{pass} = 1$ dB
- $A_{stop} = 80$ dB
- $F_{pass} = 1$ MHz
- $F_{stop} = 1.2$ MHz

The designed Butterworth filter is shown in figure 3.4. The resulting signal $y(n)$ will be repre-

sented as:

$$y(n) = x'_{win}(n) * h(n) \tag{3.4}$$

where $h(n)$ is the impulse response of the designed filter and $*$ represent the convolution operator.

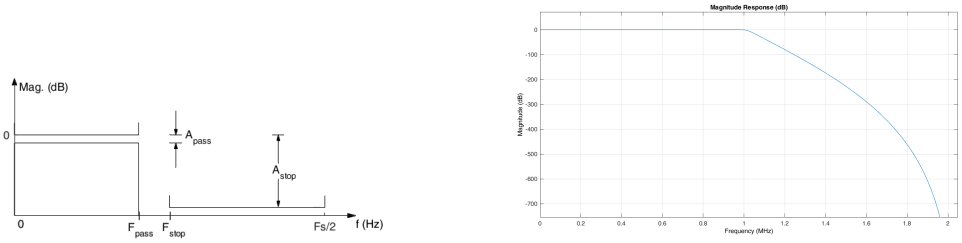

(a) Filter parameters.

(b) Matlab filter design.

Figure 3.4: Butterworth filter design.

3.1.3 Threshold Estimation

To optimize tone detection and identification, the spectral magnitude components $|X_f(f)|$ of the analyzed signal are compared to a given threshold X_0. Assuming that in the absence of tones, both the real and imaginary FFT components follow a zero-mean Gaussian distribution, the spectral magnitude follows a Rayleigh distribution. In this context, the threshold X_0 can be calculated using the formula [3]:

$$X_0 = F_R^{-1}(1 - PFA, \sigma) \tag{3.5}$$

Where F_R is the Cumulative Distribution Function (CDF) associated with the Rayleigh distribution with parameter $\sigma = \frac{E(|X_f(f)|)}{\sqrt{\pi/2}}$ and probability of false alarm $PFA = 10^{-6}$.

3.1.4 Peaks Filtering

The estimated threshold X_0 is then applied to filter out the frequency peaks (or tones) present in our signal. The detection of such components is done by identifying the amplitudes in the magnitude spectrum that exceed a predefined threshold, expressed by the following formula:

$$|X_f(f)| > X_0 \tag{3.6}$$

where X_0 is the selected threshold used for filtering from Equation 3.5 and $|X_f(f)|$ represents the magnitude of the signal spectrum, calculated as

$$|X_f(f)| = \sqrt{Re(X_f)^2 + Im(X_f)^2} \tag{3.7}$$

3.1.5 Peaks Detection and Satellite Identification

The algorithm developed is based on the principle that each satellite transmits a set of 9 spectral peaks equally spaced by 44 kHz, as mentioned in Section 2.2.2. The frequency of each detected peak is then compared to the frequencies of all other peaks. The difference $d_{i,j}$ between the two peaks is calculated by the following equation:

$$\mathbf{d_{i,j}} = \left| \hat{f}_i - \hat{f}_j \right| \quad \forall\, i > j \tag{3.8}$$

where $\hat{f}_i$ and $\hat{f}_j$ represent the detected frequencies of the spectral peaks i and j, respectively.

The calculated difference $d_{i,j}$ is then compared to 44 kHz or its multiples, as this is indicative of whether the detected peaks belong to the same satellite, given that a single satellite may not have all 9 peaks visible.

This method makes it possible to identify and group peaks belonging to the same satellite. However, the analysis is not limited to using a single threshold, X_0, to filter out peaks of interest. Instead, a *multi-threshold* strategy is used. If the number of detected satellites does not reach the predetermined minimum number, the strategy includes the option to progressively lower the detection threshold. Each reduction allows the search for new peaks to be extended closer and closer to the noise floor.

3.2 Tracking

After the initial signal acquisition phase, the system enters the tracking phase, an ongoing process that is critical to maintaining a stable and accurate connection to the satellite. In a standard GNSS system, while acquisition provides an approximate indication of signal frequency and phase, tracking is primarily concerned with refining these parameters and ensuring a consistent connection over time.

In the specific context of this thesis, which focuses on Starlink signals, tracking must overcome

different challenges than those typical of positioning systems. Unlike GPS and other GNSS systems, which are designed with built-in tracking capabilities, Starlink's unmodulated tones do not inherently support this function.

To address these complexities, the custom Matlab tool developed uses a two-stage tracking algorithm. This includes a third-order phase-locked loop (PLL) supported by a second-order frequency-locked loop (FLL). The block diagram of the implemented tracking algorithm is shown in Figure 3.5.

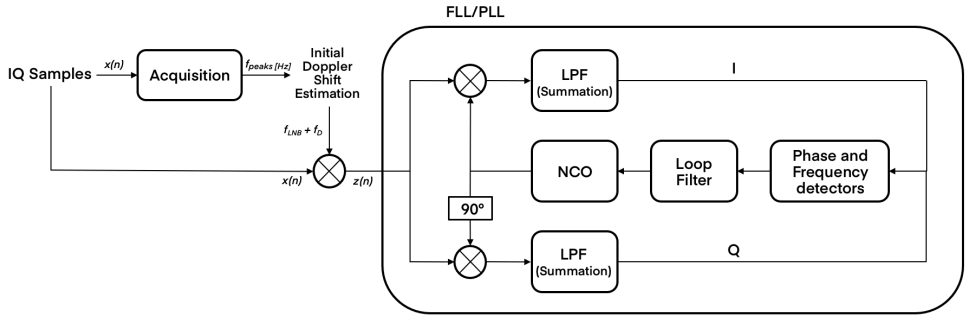

Figure 3.5: Block diagram of the Tracking phase.

3.2.1 Frequency and Phase Lock Loop

FLL and PLL are two types of control loops commonly used in Doppler shift-based satellite tracking. The FLL is responsible for constantly adjusting and refining the frequency estimates obtained during the acquisition phase, eliminating frequency errors between the input signal and the Numerically Controlled Oscillator (NCO). The PLL, on the other hand, is responsible for monitoring and locking the phase of the input signal to the locally generated phase. These loops operate in a complementary manner, often sharing the same integrators to optimize performance. In this context, the NCO generates a complex local carrier signal that is used to correct the next burst of input IQ data.

Initially, the FLL is prioritized, since chasing the phase when a large frequency error exists is ineffective. The FLL provides accurate frequency locking, which is particularly important when initial frequency errors are large, due to its wide pull-in range. The latter represents the frequency offset range within which the FLL can successfully lock onto the desired frequency ($1/T$, with T integration time). Once the frequency has been acquired and stabilized, a "constant" phase error remains. At this point, the PLL is enabled to track and refine this phase: by

tracking the phase, the frequency is also implicitly maintained. Once phase locking is achieved, the FLL can be turned off, putting the PLL in charge of maintaining accurate phase tracking. However, in applications with high dynamic stress, both loops may remain active for the duration of tracking [3].

Key components are *Discriminators*, which measure both the phase error (φ_e) and the frequency error (f_e) between the input signal and the locally generated signal. These errors are then used to adjust the NCO. They are represented by:

$$\varphi_e = (2\pi)^{-1} \operatorname{atan2}(Q_n, I_n) \tag{3.9}$$

$$f_e = (2\pi T)^{-1} \operatorname{atan2}(Q_n I_{n-1} - Q_{n-1} I_n, I_n I_{n-1} + Q_n Q_{n-1}) \tag{3.10}$$

Another critical component is the *Loop Filter*, denoted as $F_{pll}(s)$ for the PLL and $F_{fll}(s)$ for the FLL. This filter is used to damp oscillations and minimize errors in the system. Specifically, the phase error is processed through a second-order loop filter $F_{pll}(s)$, while the frequency error is processed through a first-order loop filter $F_{fll}(s)$. These filters are designed to reduce noise and provide accurate estimates of the phase and frequency of the input signal. These filters are described as:

$$F_{pll}(s) = \left(w_{0p}^3 + 1.1 w_{0p}^2 s + 2.4 w_{0p} s^2 \right) / s^2 \tag{3.11}$$

$$F_{fll}(s) = \left(w_{0f}^2 + \sqrt{2} w_{0f} s \right) / s \tag{3.12}$$

where the coefficients are typical filter values for the application concerned.

The performance of these loop filters depends on their natural frequencies, $w_{0p} = (0.7845)^{-1} B_{0p}$ and $w_{0f} = (0.53)^{-1} B_{0f}$, for the PLL and FLL, respectively. These natural frequencies are directly related to the equivalent noise bandwidths (B_{0p} for the PLL and B_{0f} for the FLL). Both B_{0p} and B_{0f} have a significant impact on thermal noise and dynamic stress. Higher values of B_0 allow faster error correction, but introduce more noise. Conversely, lower values reduce noise but slow down the error correction capabilities of the system.

3.2.2 Tracking Algorithm

Frequency correction with estimated acquisition frequency

First, each data burst is subjected to a frequency correction before entering the tracking phase. This correction is performed using a frequency value that is the sum of two components: the Doppler value estimated during the acquisition phase (f_D) and the LNB frequency error (f_{LNB}). The latter is used to refine the initial accuracy of the LNB. Note that with a high precision LNB, f_{LNB} may be zero.

Considering a burst of IQ data over time $x(n)$, the frequency correction can be expressed as:

$$z(n) = x(n) \cdot e^{-j\,2\pi(f_{LNB}+f_D)nT_s} \tag{3.13}$$

PLL and FLL implementation

Once the IQ data burst has been corrected from the initial estimate obtained in the acquisition phase, the tracking algorithm has been implemented as in [3]: a NCO generates a complex local carrier signal of duration T (called the integration time), which is multiplied by a burst of the input signal of equivalent duration. The results on the real and imaginary branches are then filtered by a Low Pass Filter (LPF) through a sum over T to obtain a complex signal $(I_n + jQ_n)$. The phase of this signal represents the phase difference between the local carrier signal and the incoming tone. The resulting signal is used by a phase discriminator and a frequency discriminator to calculate the phase error φ_e and the frequency error f_e, respectively. The phase error φ_e is then filtered by a second order loop filters $F_{pll}(s)$ and the frequency error is filtered by a first order loop filter $F_{fll}(s)$ to reduce noise and produce an accurate estimate of the phase and frequency of the input signal. The output of the filter is then fed into the NCO, which changes the phase and frequency of the local carrier to match those of the incoming signal. The output of the NCO is then mapped into cosine and sine functions to provide an accurate carrier replica of the received signal.

3.2.3 Thermal Noise and Dynamic Stress

Thermal noise and dynamic stress are a significant variables in the satellite tracking process, especially in applications involving rapid motion or sudden changes in direction. These factors can significantly affect the accuracy with which phase and frequency errors are tracked by PLL and FLL. In particular, the error due to thermal noise is directly related to the equivalent noise

bandwidth, B_0, and inversely related to the integration time, T. In contrast, the dynamic stress is determined solely by B_0.
Increasing B_0 reduces dynamic stress, but at the cost of increasing thermal noise for both phase and frequency. Instead, by affecting the integration time, a shorter T allows for the capture of high-frequency errors that are common in high-dynamic-stress scenarios. However, too short a value of T can reduce the system's ability to effectively filter out thermal noise. In summary, the choice of B_0 and T must be made to balance the need to reduce both dynamic stress and thermal noise. This decision is decisive to ensuring stable and accurate tracking in the highly dynamic operating environment of LEO satellites. Details regarding the specific values of B_0 and T will be discussed in chapter 4.

3.3 Visibility Predictor

As discussed in section 2.1.6, in Doppler-effect positioning systems using SOOPs, the ephemerides of satellites are not available to determine their exact position and velocity. The alternative is to use TLE files, public data distributed by NORAD.

As part of this thesis project, a satellite visibility prediction software has been developed. Using TLE files specific to the Starlink satellites and the SGP-4 simplified perturbation model, the software provides information about the position and velocity of the Starlink satellites at a given time. This allows us to effectively filter the satellites and generate a sky plot referenced to the geographic location of our receiver. The block diagram of the developed Visibility Predictor is shown in Figure 3.6.

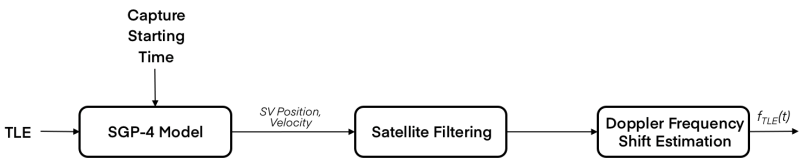

Figure 3.6: Block diagram of Visibility Predictor.

3.3.1 TLE Analysis

Each TLE file is associated with a *starting time*, which attests to the period of validity and reliability of the information contained in the file. In the implementation of the SGP-4 model, the inputs of the model are the TLE file and a time offset from its starting time. This offset makes it possible to analyze the position and the speed of the satellites at the exact time of our acquisition. For example, if the TLE of a specific satellite has a *starting time* set to May 23, 2022 at 16:54:07 UTC, and we want to analyze data (satellite position and velocity) for May 24, 2022 at 08:35:00 UTC, the offset to be applied will be +15 hours, 40 minutes and 53 seconds.

3.3.2 Satellites Filtering

This analysis assumes that accurate receiver position information is available. This assumption is discussed further in the chapter 5, where possible applications and implications of this assumption are explored.

The algorithm examines all the satellites listed in the TLE file and for each time interval in the desired acquisition interval it compares their position with that of the receiver in use.

The SGP-4 model implementation outputs the position and velocity of the satellite in the TEME (True Equator Mean Equinox) coordinate system. These coordinates are converted to the Earth-Centered, Earth-Fixed (ECEF) coordinate system. This step is essential to calculate the vector **v** that connects the receiver to the satellite:

$$\mathbf{v} = \begin{pmatrix} x\_rec\_sat \\ y\_rec\_sat \\ z\_rec\_sat \end{pmatrix} = \begin{pmatrix} x\_sat \\ y\_sat \\ z\_sat \end{pmatrix} - \begin{pmatrix} x\_rec \\ y\_rec \\ z\_rec \end{pmatrix} \tag{3.14}$$

The vector v is then converted to topocentric coordinates to facilitate the calculation of azimuth, elevation, and distance. These parameters are then used to apply a filter to the satellites based on a predetermined elevation mask referenced to the position of the receiver.

3.3.3 Doppler Frequency Shift Estimation

After identifying the list of satellites in the receiver's vicinity that fall within the predefined elevation mask, the Doppler frequency shift for each satellite is estimated. In this way, each Starlink satellite is assigned a specific Doppler shift for the entire acquisition period.

For this purpose, the received frequency f_R is calculated for each satellite at any time during the acquisition phase:

$$f_R = f_T \left(1 - \frac{v_r \cdot a}{c}\right) (Hz) \tag{3.15}$$

where

- f_R is the received frequency (Hz)
- f_T is the transmitted frequency (Hz)
- v_r is the Satellite-to-User relative velocity (m/s)
- a is the unit vector pointing along line-of-sight from user to SV
- c is the speed of light (m/s)

The Doppler frequency shift is then obtained:

$$\Delta f = f_R - f_T (Hz) \tag{3.16}$$

4

Experimental Results

After a detailed description of the methods and approaches presented in chapter 3, this chapter is dedicated to the presentation and analysis of the experimental results obtained. As mentioned before, the analysis in this thesis is based on real data collected by the Starlink satellites. The first section will introduce the files used throughout the thesis project. Subsequent sections will present the results related to the acquisition, tracking, and visibility prediction phases applied to the SOOPs provided by the Starlink satellites.
In this chapter, various graphs, tables, and other forms of visual representation will be used to illustrate the effectiveness and performance of the proposed methods.

4.1 File Setup

Two different Starlink captures provided by the European Space Agency (ESA) were used for this thesis project; they have a bandwidth of 4,096 MHz, but differ significantly both in the hardware used to capture them and in the signal quality. Each capture was formatted with a resolution of 64 bits per sample, divided into 32 bits for the I-component and 32 bits for the Q-component.

First capture: May 2022

The first capture, taken in May 2022, was made with inexpensive hardware. This data set, of 91,20 seconds, is characterized by many tones in the signal, which makes it useful for the acquisition phase. However, it is important to note that this capture is also quite noisy, which limits its use to the acquisition phase only.

Second capture: March 2023

In contrast, the second capture, from March 2023, was taken with more advanced hardware. This dataset has fewer tones than the first, but provides a generally cleaner signal. Although this signal also has a duration of about 90 seconds, it only has a good SNR in a short portion of the signal that lasts a few seconds. As a result, it was used primarily for the tracking phase.

The specifications of the two files are summarized in Table 4.1.

Specification	**First Capture (May** 2022**)**	**Second Capture (March** 2023**)**
Hardware Quality	Inexpensive	Advanced
Duration (seconds)	91.20	$\sim$ 90
Signal Characteristics	Many tones, Noisy	Fewer tones, Cleaner
Main Use	Acquisition Phase	Tracking Phase
Notes	Limited to acquisition due to noise	Good SNR only for a few seconds

Table 4.1: Specifications for data capture 1 and 2.

TLE Files

TLEs provided by the NORAD were used to calculate an estimate of the Doppler effect on the signals using the SGP-4 model. The associated TLE files were included in the data capture package provided by the ESA.

4.2 Acquisition

The acquisition phase represents the first block in the process outlined in the diagram in Figure 3.1 and plays a key role in the analysis and processing of Starlink SOOPs. During this phase, the satellites are identified and separated by the constraints explained in the previous chapters 2 and 3. For this phase, it was decided to use the data from the first capture, which contains enough satellites to allow the development of a satellite identification tool.

4.2.1 Estimation of Acquisition Window Length

Before proceeding with any signal processing, it is necessary to determine the optimal acquisition window length T_{best}. As described in the chapter 3, the choice of window length is critical for several reasons, including computational complexity, noise control, and spectral leakage mitigation. For this purpose, the total capture of 91.20 seconds was divided into three blocks of approximately 30 seconds each. This subdivision allowed a clearer understanding of the relationship between the maximum peak and the estimated threshold (and thus the SNR) in different time intervals of the capture.

From the graph shown in Figure 4.1a, a constant observation can be made in each block: the ratio of the maximum peak to the estimated threshold tends to stabilize after a window length of $T_{best} = 10$ ms. This observation guided the decision to set the acquisition window length at 10 ms. It was not considered useful to extend the it further, since the graph does not show a significant increase in the ratio of maximum peak to noise. After selecting the 10 ms capture time, further analysis was performed on the entire capture. The results of this analysis are shown in the graphs in Figure 4.1b, which displays the maximum peak values, estimated thresholds, and their ratio over the duration of the capture.

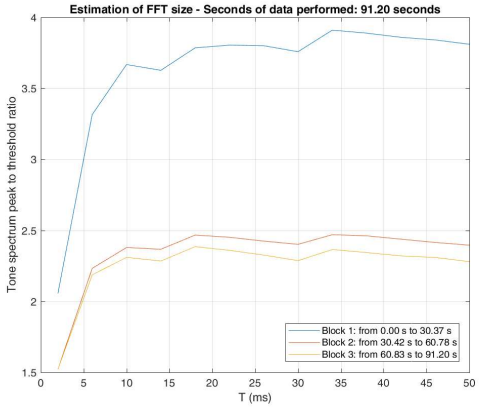

(a) Maximum Peak to Threshold Ratio

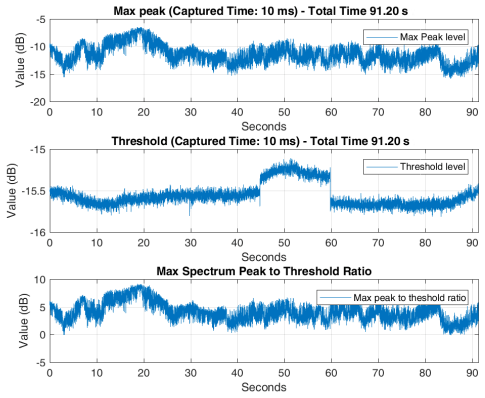

(b) Entire Capture with 10 ms Acquisition Window Length

Figure 4.1: Analysis of the maximum peak to threshold ratio.

As shown in the graph in Figure 4.1b, the ratio of the maximum peak to the estimated threshold is always above 0 dB for most of the duration of the capture. This means that it is possible to identify a peak that is distinguishable from the noise for the entire duration of the acquisition.

4.2.2 Signal Filtering

Once the optimal acquisition window length has been estimated, the next step is to prepare the signal for the forthcoming analysis. This preparation involves a series of signal processing operations that are carefully selected to improve signal quality, reduce noise, and isolate relevant information, as described in Section 3.1.2.

Fix LNB accuracy

During the signal acquisition phase, the accuracy of the LNB used may introduce a frequency error f_{LNB}. As discussed in the Chapter 3, the first step to correct this problem is to adjust the frequency of our input IQ signal by frequency shifting. The frequency correction is done according to the equation 3.1.

Looking at figure 4.2, we can see that in the original spectrum, the tones are shifted by 800 kHz due to the accuracy of the LNB. After applying the frequency correction, it can be seen that the tones are now correctly centered in the baseband, demonstrating the effectiveness of the applied correction.

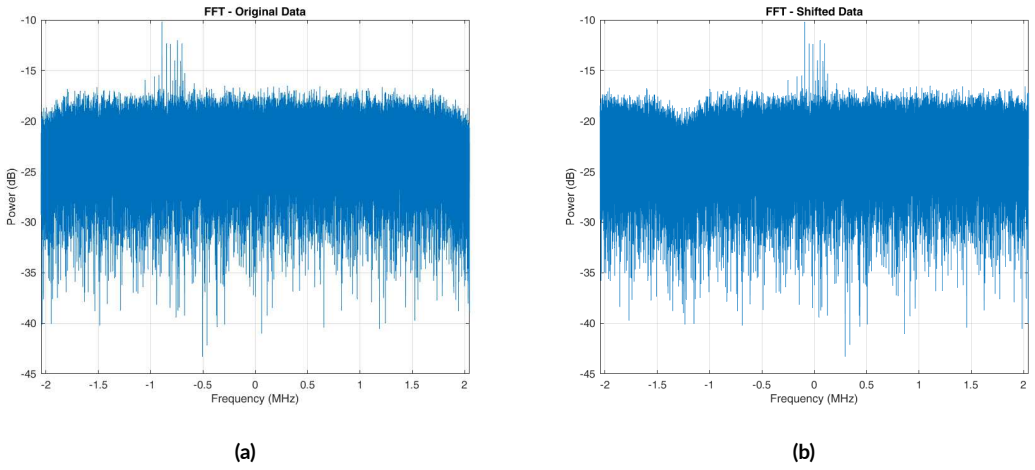

Figure 4.2: FFT of (a) the original signal and (b) the shifted Signal.

Windowing and Butterworth filter

After the frequency correction, the signal goes through further processing steps. First, a Hann window is applied to the signal according to equation 3.2. Next, the signal is filtered using a Butterworth filter as described in equation 3.4.

From the figure 4.3 we can observe the results of these preprocessing operations. In particular, we can see that after the filter is applied, the signal spectrum appears filtered at the desired frequencies, eliminating unwanted frequency components and ensuring a cleaner, more defined signal for the following steps.

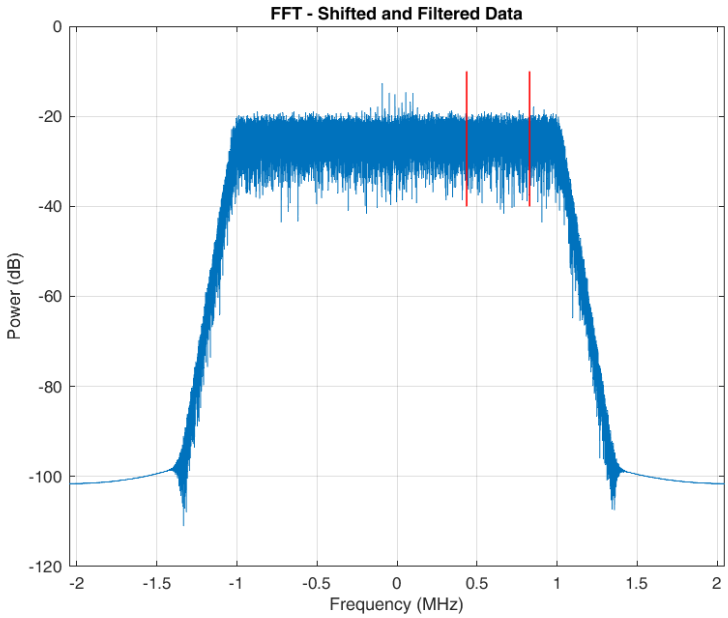

Figure 4.3: Butterworth filter application.

4.2.3 Threshold Estimation

Now that the signal has been processed and filtered, it is possible to proceed with the threshold estimation. As explained in Section 3.1.2, the filter is designed to operate over a 2 MHz band. This specific choice ensures the presence of a no-peaks portion of the spectrum, which becomes essential in the threshold estimation stage. In the graph shown in Figure 4.3, this portion of the spectrum is clearly highlighted by the red interval. A detailed representation of this interval is shown in the Figure 4.4a.

With the information extracted from this part of the spectrum, it is then possible to proceed to the application of the Equation 3.5, which is responsible for determining the threshold. The Figure 4.4b shows the Rayleigh CDF along with the estimated threshold (in red), obtained considering a probability of false alarm PFA $= 10^{-6}$. The estimated threshold value obtained is $-17{,}55$ dB.

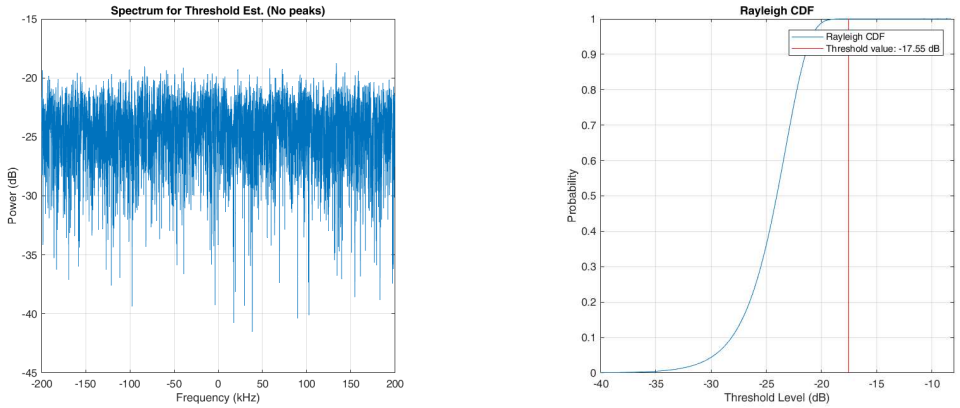

(a) Portion of the spectrum for threshold estimation

(b) Rayleigh CDF

Figure 4.4: Threshold estimation analysis.

4.2.4 Peaks Filtering and Analysis

Based on the methods proposed in the previous chapter, the next step in signal processing is to identify and analyze frequency peaks. After determining the optimal acquisition window length T_{best} and establishing an appropriate threshold X_0, it is then possible to effectively filter and identify the peaks (or tones) present in our signal.

Figure 4.5 shows the spectrum with all detected peaks. Each peak is distinguished by the use of colored dots, where each color represents a different satellite. This visualization makes it easy and intuitive to identify the satellite to which each peak belongs. Looking at the figure, it can be seen that three different satellites have been identified, highlighted by the different colors used to represent each satellite.

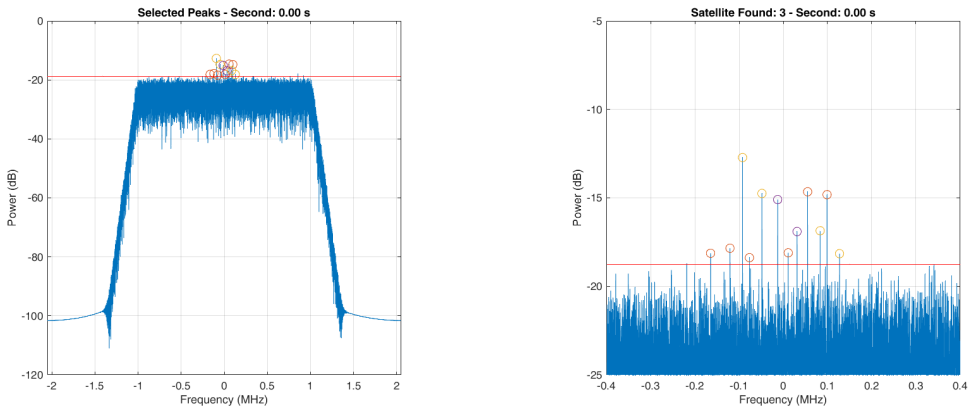

(a) (b)

Figure 4.5: Identified spectral peaks (a) and magnification (b) of 10 ms window length

More specifically, the following three figures show the distribution of the peaks for each satellite:

- Figure 4.6a shows 6 distinct peaks associated with the first satellite. This indicates a strong presence of the satellite in the field of view, although not all 9 theoretical peaks are visible. The missing tones could be under the noise floor or superimposed by interfering signals.
- Figure 4.6b shows the second satellite, with 4 peaks identified. Again, not all of the theoretical peaks are present.
- Figure 4.6c shows the third satellite with only 2 peaks identified. This could indicate a more distant location of the satellite or more interference at the frequencies corresponding to the missing peaks.

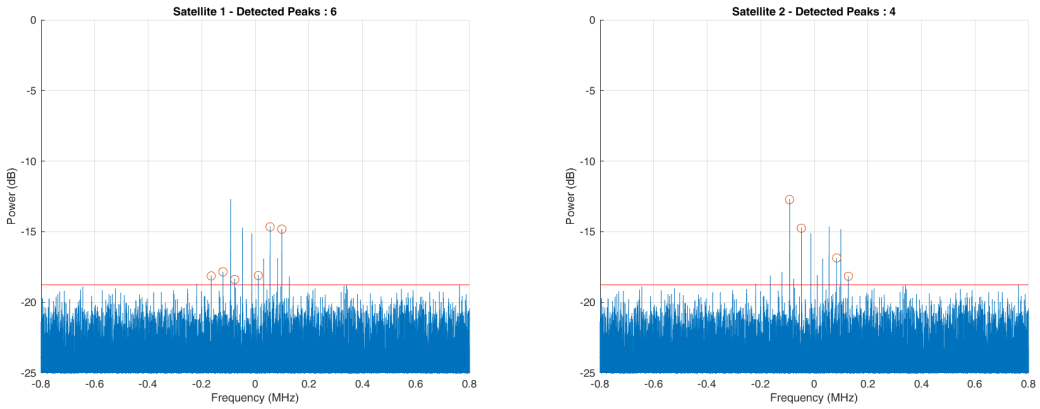

(a) Spectral peaks of satellite 1.

(b) Spectral peaks of satellite 2.

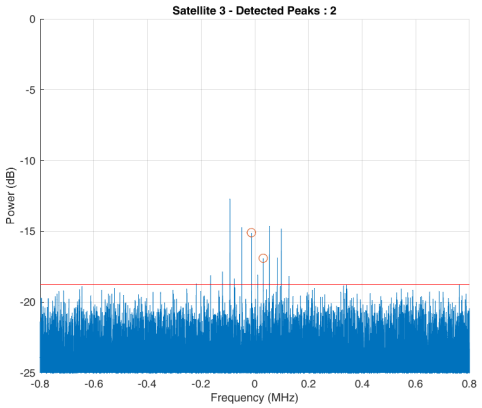

(c) Spectral peaks of satellite 3.

Figure 4.6: Spectral peaks identified for (a) satellite 1, (b) satellite 2, (c) satellite 3.

4.2.5 Multi-Threshold Analysis

The multi-threshold strategy is essential for detecting peaks that might otherwise be hidden under the noise floor, providing a complete and detailed view of the situation. It is based on the idea of progressively varying the detection threshold to closely examine the signal behavior and identify additional peaks that might remain hidden using a single threshold. Multi-threshold analysis uses a strategy where the threshold is lowered by steps of $-0{,}15$ dB. This is done until the desired number of satellites is reached or until the maximum value defined for the threshold is reached.

Figure 4.7 shows the output of the analysis performed in Matlab, illustrating all the steps of the multi-threshold analysis.

```
STARTING ACQUISITION..
Acquisition Capture Time: 10 ms

Probing data (starlink data/Starlink_4096ksps_11325MHz_20220524-083500UTC)...

Estimated Threshold: -17.55 dB

Case 0 - Threshold: -17.55 dB: Satellites detected: 3. (Decreasing Threshold)
Case 1 - Threshold: -17.70 dB: Satellites detected: 3. (Decreasing Threshold)
Case 2 - Threshold: -17.85 dB: Satellites detected: 3. (Decreasing Threshold)
Case 3 - Threshold: -18.00 dB: Satellites detected: 3. (Decreasing Threshold)
Case 4 - Threshold: -18.15 dB: Satellites detected: 3. (Decreasing Threshold)
Case 5 - Threshold: -18.30 dB: Satellites detected: 3. (Decreasing Threshold)
Case 6 - Threshold: -18.45 dB: Satellites detected: 3. (Decreasing Threshold)
Case 7 - Threshold: -18.60 dB: Satellites detected: 3. (Decreasing Threshold)
Case 8 - Threshold: -18.75 dB: Satellites detected: 3. (Decreasing Threshold)
Max Threshold Value Reached.
```

Figure 4.7: MATLAB Output of multi-threshold analysis

In the next four graphs in figure 4.8, it can be seen that as the threshold is lowered in increments of $-0{,}15$ dB for each step, new peaks are found. These emerging peaks are then assigned to their respective satellites, providing a more detailed and complete view of satellite presence in the analyzed spectrum.

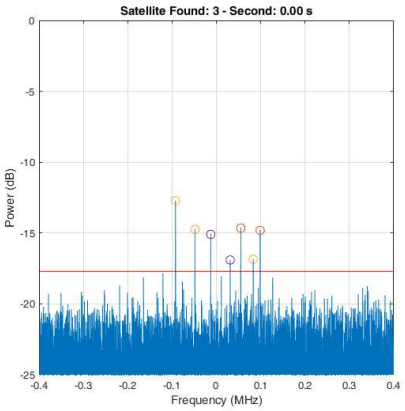

(a)

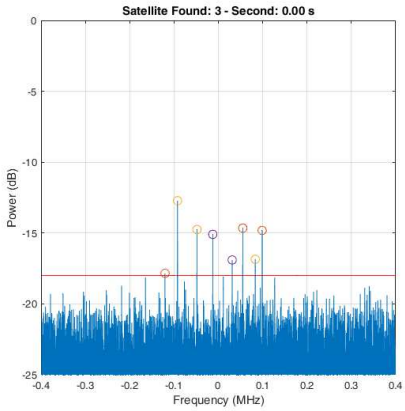

(b)

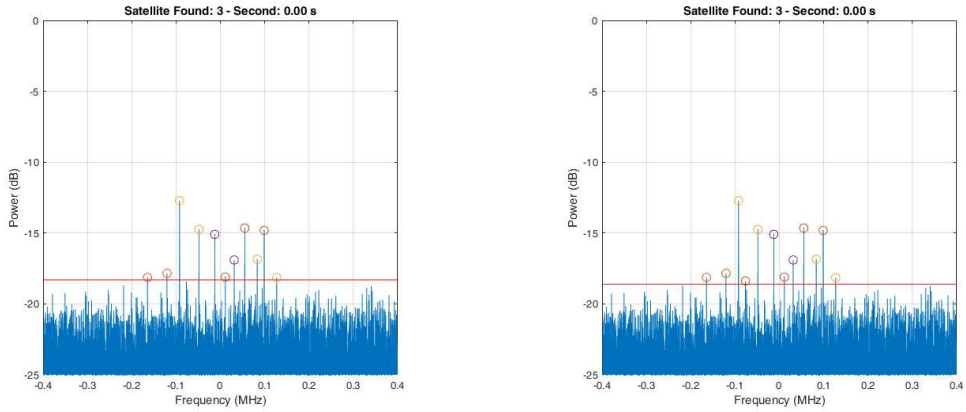

(c) (d)

Figure 4.8: Multi-threshold analysis steps

4.3 Tracking

After the signal acquisition phase, the system enters the tracking phase, which is necessary to maintain a stable and accurate link with the satellite. For the this phase, it was decided to use the second file provided by ESA. This decision was motivated by the overall lower quality of the first file, which was obtained with a cheaper acquisition setup and therefore more subject to noise. Although the second acquisition, made with a more advanced setup, shows a clear improvement in terms of noise reduction, it does not show the same peak density found in the first acquisition.

The file provided by ESA contained a single prominent peak with a high dB value. This particular peak was carefully monitored as it represents the dynamics of a transmission in LEO orbit. The results of this analysis will be compared later with typical LEO values presented in Chapter 2.

4.3.1 Tracking Parameters

As mentioned in the previous chapter, the choice of integration time T plays a key role in tracking. It must achieve a trade-off between noise reduction and the ability to detect high-frequency errors. For the tracking phase, an integration time of $T = 2$ ms was chosen. This choice allowed for a larger initial pull-in range, which is essential for the initial tracking phase. A characteristic of the proposed tracking method is the joint use of a FLL and a PLL. As described in the pre-

vious chapter, the FLL is operational from the beginning of the acquisition, while the PLL is activated only after 0.5 second from the beginning, when the frequency lock is reached. The optimal balance between noise reduction and dynamic stress tolerance was achieved by selecting the B_{0p} and B_{0f} bands at 15 Hz as the equivalent noise band for the PLL and FLL, respectively. The Table 4.2 summarizing the parameters chosen for the tracking phase is presented below:

Parameter	**Value**
Integration Time T	2 ms
PLL Equivalent Noise Bandwidth B_{0p}	15 Hz
FLL Equivalent Noise Bandwidth B_{0f}	15 Hz
PLL Enabling	After tracking lock

Table 4.2: Tracking parameters.

Figure 4.9 shows the spectrum of the signal considered for this phase, provided by ESA. The signal processing and filtering techniques described in the acquisition section have been applied to this signal, resulting in the output of the frequency f_D that will be tracked during this phase. As it can be seen, from the spectrum, it is already centered in the baseband, so no frequency correction is needed, and f_{LNB} is set to 0. It is also evident that there is only one peak in the spectrum, indicating the presence of a single satellite.

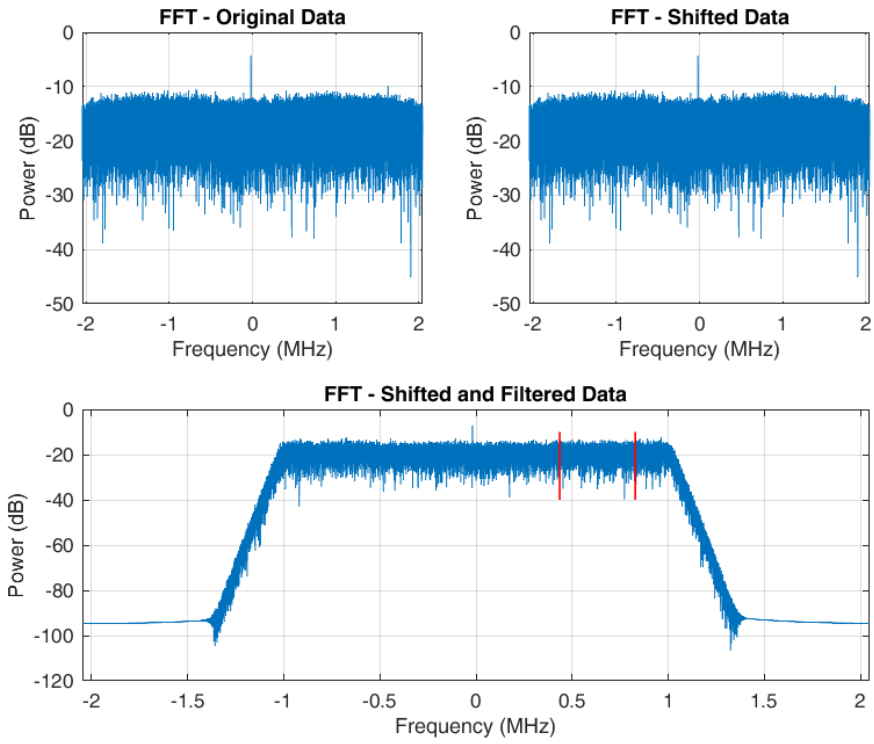

Figure 4.9: Analysis of the spectrum and filtering of the second capture.

4.3.2 Doppler Frequency Shift Estimation

Figure 4.10 shows the results of 1 second of tracking. To provide feedback on the validity of the tracking algorithm, in addition to the estimated Doppler frequency shift, the real value obtained by a multiple-acquisition is also shown (labelled "max method" in the legend). This value is calculated directly from the spectrum of our signal by taking the maximum value of the FFT. It is subject to a resolution defined by:

$$f_{res} = \frac{Bandwidth}{sizeFFT} = \frac{4{,}096 \text{ MHz}}{8192} = 500 \text{ Hz} \tag{4.1}$$

This justifies the presence of the stepped signal shown in the figure, which is essential to analyze the trend of our signal and evaluate the effectiveness of the tracking system.

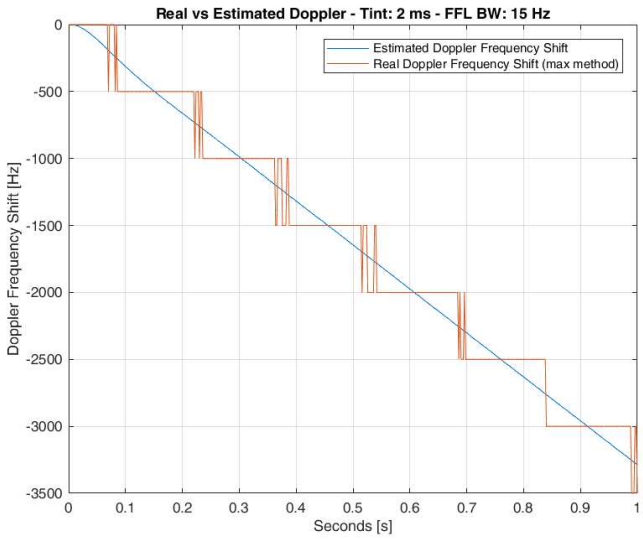

Figure 4.10: Estimated Doppler frequency shift with the developed Tracking Loop.

From the graph, we observe an approximate Doppler rate of 3,3 kHz/s, a value consistent with those associated with LEO orbits reported in the Table 2.3.

4.3.3 FLL and PLL Results

Figure 4.11a shows the I and Q components entering the discriminators. These components can be observed in the block diagram shown in figure 3.5. From the figure, it is clear that the tracking lock can be identified from the instant when the I and Q components become distinguishable in time. The figures 4.11b and 4.11c illustrate the results obtained by the discriminators, both PLL and FLL. For analytical purposes, Figure 4.11d shows the normalized histogram of the number of error for FLL, which represents the probability distribution. Examining the distribution in more detail, it can be seen that the mean of the errors is close to zero, confirming that most of the errors are minimal and that the tracking algorithm is working as expected. This behavior is consistent with a well-performing tracking algorithm.

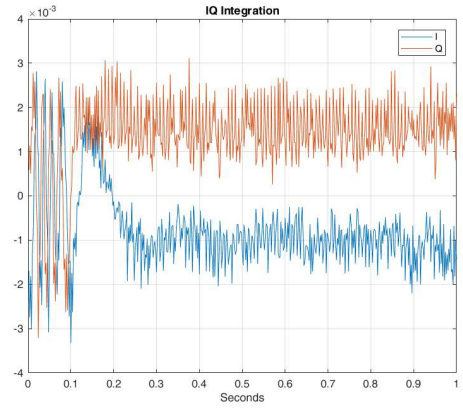

(a) IQ Component entering the discriminators.

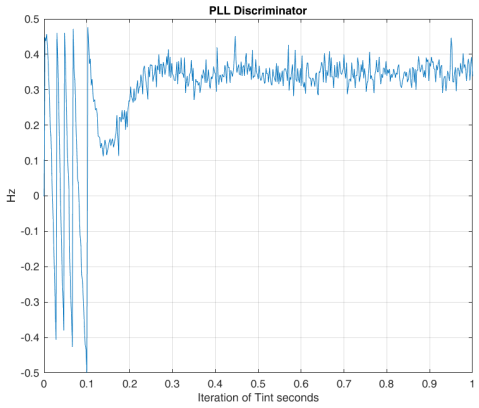

(b) PLL discriminator result.

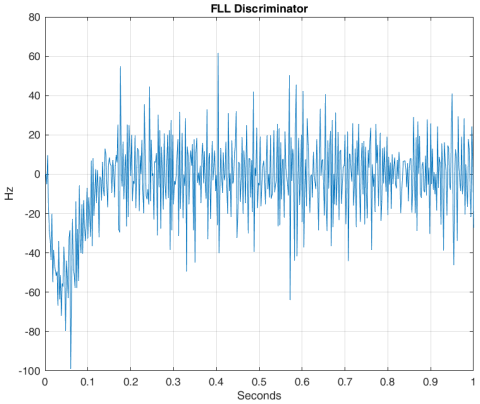

(c) FFL discriminator result.

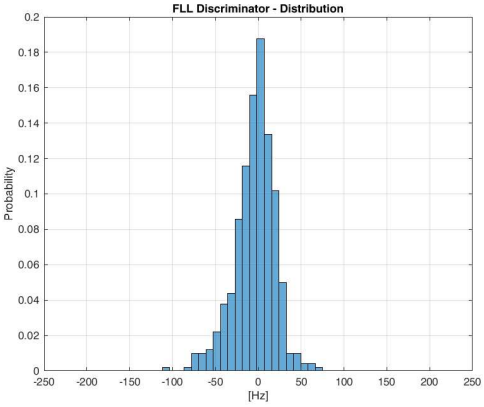

(d) FFL errors distribution.

Figure 4.11: PLL and FLL results.

4.3.4 Simulated Continuous Wave Analysis

To further evaluate the performance of the developed tracking loop, a simulated signal was generated. This signal consists of a Continuous Wave (CW) with additional AWGN noise, designed to emulate as closely as possible the structure of a real signal. The objective was to test the system under different conditions and to examine its operational limitations. An instant of the generated signal in frequency domain is shown in figure 4.12.

The simulated CW signal $c(n)$ can be defined by the following formula:

$$c(n) = A \cdot \exp\left(j \cdot (2\pi f n T_s + \varphi)\right) + w(n) \tag{4.2}$$

where:

- A is the amplitude of the tone
- f is the frequency of the tone
- φ is the initial phase,
- $w(n)$ is the AWGN noise

In our case, the simulated signal has a frequency f defined by the variable tone frequency and a phase φ initially set to 0.

From the figure 4.12 we can see a peak centered on zero, above the noise level. This property is similar to the one observed in the real signal shown in the previous figure. The developed tool used to generate this signal uses the parameters described above, among others, to achieve an accurate simulation of the capture environment.

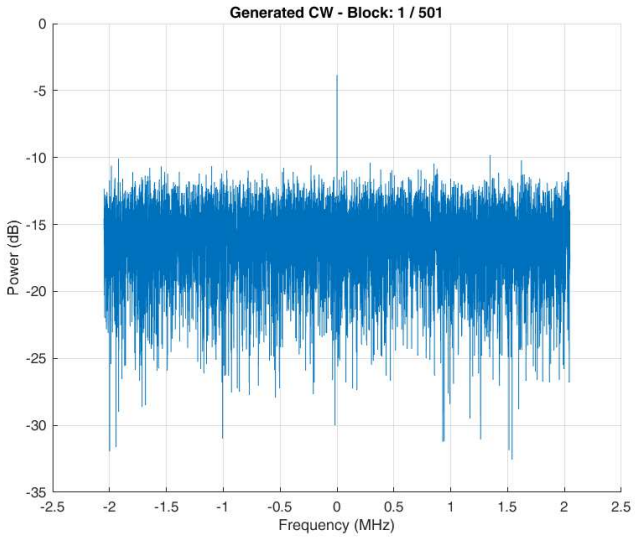

Figure 4.12: CW generated for the simulation

Pull-in Range of FLL

The first test was performed to observe the behavior of the system with respect to the pull-in range of the FLL, defined in Section 3.2.1. Assuming that the acquisition phase provided a frequency estimate f_D that was not perfectly accurate, the CW signal was then generated with a non-zero initial frequency offset.

Based on the discussions in previous chapters, the expected pull-in range for the FLL in our system is approximately $\frac{1}{T} = 500$ Hz (i.e., a range of ± 250 Hz), and the Doppler shift rate

limit for a Starlink satellite in LEO orbit is 5 kHz/s. For the simulation the Doppler shift rate has then been set to its maximum value.
Given these parameters, the tracking loop could effectively track the signal if the CW was generated with an initial frequency shift falling within the range of -250 to $+250$ Hz. Figure 4.13 shows a simulation with an error in the estimated frequency f_D of -230 Hz and -260 Hz, respectively. In the first case, it is observed that the tracking loop manages to converge after a certain time, while in the second case it diverges due to an estimation error that slightly exceeds the pull-in interval. To highlight the different scenarios, only 0,4 seconds of tracking are shown.

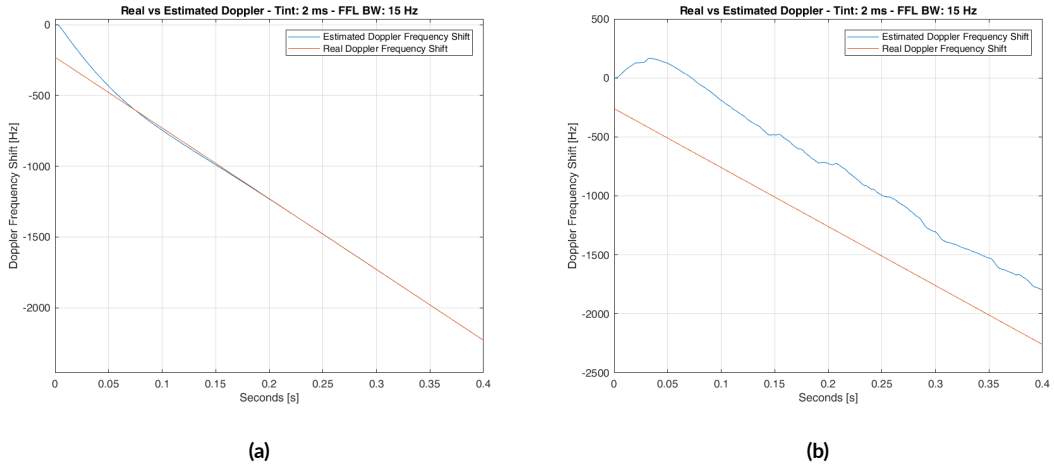

Figure 4.13: Tracking results with (a) initial frequency within the pull-in range, (b) outside the pull-in range

A further test was then performed to determine the maximum rate of Doppler shift that the system would be able to handle. With accurate initial frequency acquisition, the system can track the tone up to a Doppler shift rate of about 14 kHz/s. However, if the initial frequency acquisition is not accurate, the maximum Doppler shift rate the system can handle is reduced. It is important to note that these values are much higher than expected for a satellite in LEO orbit. However, the test was conducted with these parameters to analyze in depth the behavior of the tool in extreme situations and outside of conventional use cases. This gives us a more comprehensive view of its capabilities and potential limitations, as discussed in the next chapter.
Figure 4.14 shows the results with a Doppler shift rate of 14 kHz and 15 kHz, respectively.

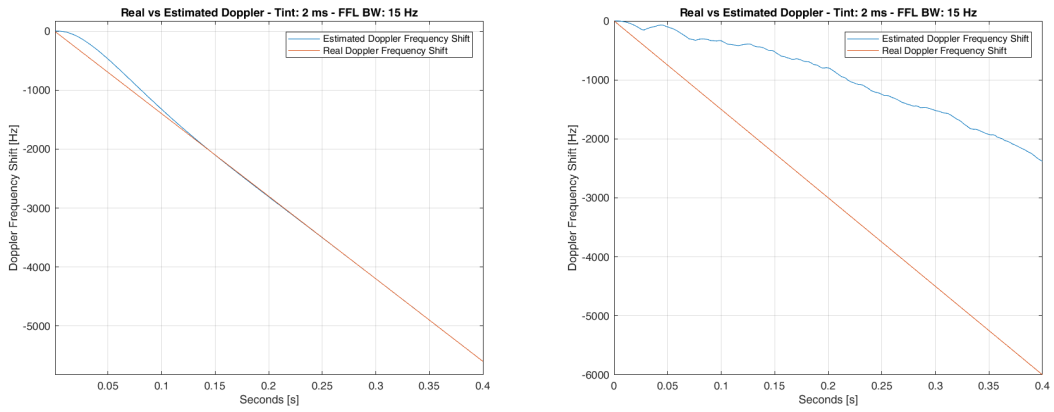

Figure 4.14: Tracking results of a signal with a Doppler rate of (a) 14 kHz, (b) 15 kHz

4.4 Visibility predictor

The tool developed for the Visibility Predictor provides detailed results on the visibility of Starlink satellites relative to the position of the receiver. In this case, data from the first capture were used, so as to make an initial comparison between the peaks detected in the acquisition and the satellites visible from the receiver on earth.

4.4.1 Satellites Visibility and Filtering

After loading the TLE file corresponding to the first acquisition, the tool extracted data from all satellites. The visibility of each satellite relative to the receiver position was then analyzed. This is done in steps of 10 seconds.
For each satellite, the *Starting Time* is determined as described in Section 3.3.1. An appropriate time offset is then applied to the SGP-4 model to align with the precise time of capture. A representation of the output of the tool developed is shown in Figure 4.15, with specific reference to the satellite named *STARLINK*-1037. In the proposed example, an offset of 5 hours, 7 minutes and 41 seconds has been applied to match the exact time of the captured signal. The estimated coordinates from the SGP-4 model and timing are shown in the figure.

```
Satellite Selected(1): STARLINK-1037
TLE Starting Time: 24-May-2022 03:27:19 UTC

Satellite Visible(1): STARLINK-1037
Time: 24-May-2022 08:35:00 UTC
Lat = 52.976863, Lon = 4.406482, Alt = 526.993678

Satellite Visible(1): STARLINK-1037
Time: 24-May-2022 08:35:10 UTC
Lat = 53.027967, Lon = 5.407950, Alt = 527.010429

Satellite Visible(1): STARLINK-1037
Time: 24-May-2022 08:35:20 UTC
Lat = 53.069913, Lon = 6.411661, Alt = 527.025123

Satellite Visible(1): STARLINK-1037
Time: 24-May-2022 08:35:30 UTC
Lat = 53.102670, Lon = 7.417178, Alt = 527.037754
```

Figure 4.15: Example of Matlab output of Visibility Predictor

The selection of satellites relative to the position of the receiver was done using a *Elevation Mask* set to 60°. The purpose of this selection is to limit the field of view to the satellites closest to the receiver, for both operational and visual purposes. In fact, without this filter there would be too many satellites in the plot, making the display less clear and cluttered. Figure 4.16 shows the SkyPlot resulting from this particular satellite filtering. In the figure, the $*$ symbol represents the initial time considered, while the related continuous line represents the predicted trajectory.

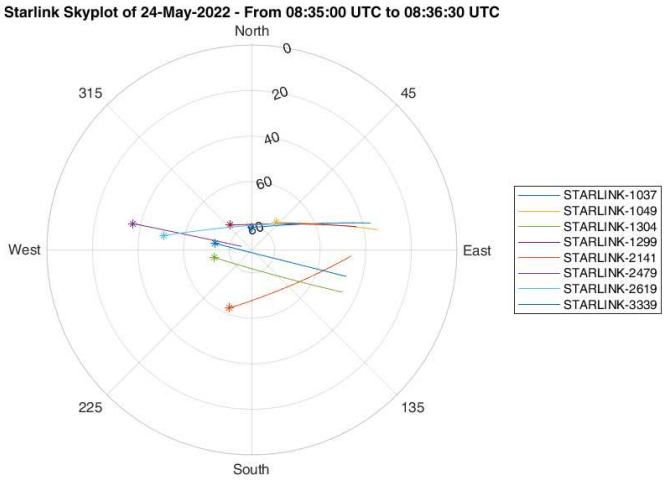

Figure 4.16: SkyPlot of the first capture analyzed

4.4.2 Doppler Frequency Shift Estimation from TLE

At each iteration, for all satellites that meet the elevation mask constraint, the frequency shift due to the Doppler effect is calculated using Equation 3.15. The result of this calculation is shown in Figure 4.17. Using the SGP-4 model and TLE files, 8 satellites were identified with their respective Doppler frequency shifts. As can be seen, the maximum Doppler shift and Doppler shift rate values appear to be consistent with those associated with Starlink satellites in LEO orbit, as described in the Table 2.3.

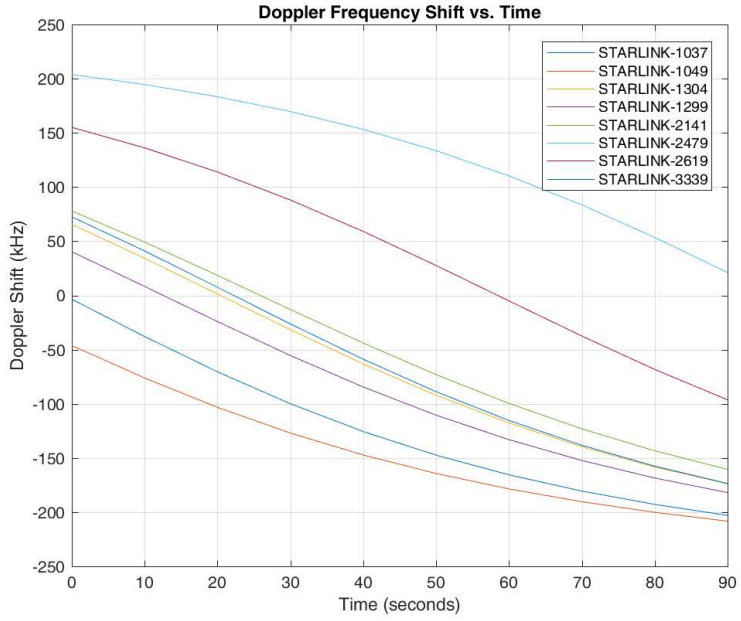

Figure 4.17: Doppler frequency shift estimated with TLEs

4.4.3 Peak Density and SkyPlot Relationship

At this point, the instants that were detected by the SkyPlot were analyzed one by one. For each of these instants, peak detection and identification was performed. As an example, Figure 4.18 shows the results for 0, 20, and 60 seconds after the start of the acquisition.

The analysis of these figures clearly shows a direct relationship between the density of the observed peaks and the position of the satellites. In particular, looking at the figure 4.18b, which shows the optimal position of the satellites with respect to their distance from the receiver, it is clear that the density of peaks is higher at this specific time. In addition, the peaks present have

a significantly higher magnitude, expressed in dB.

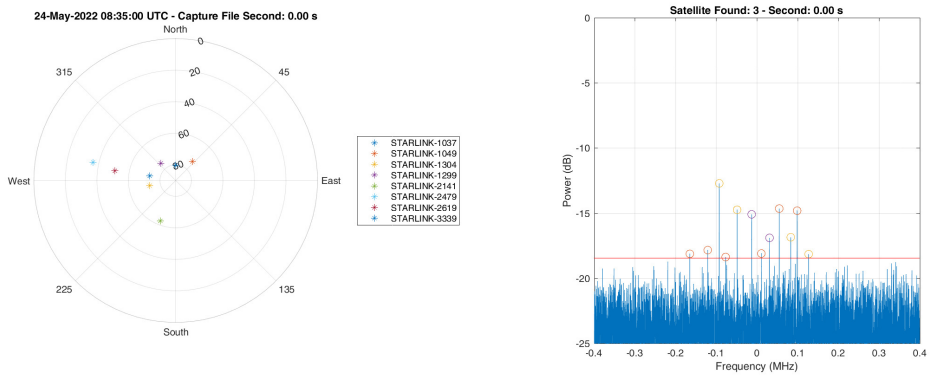

(a)

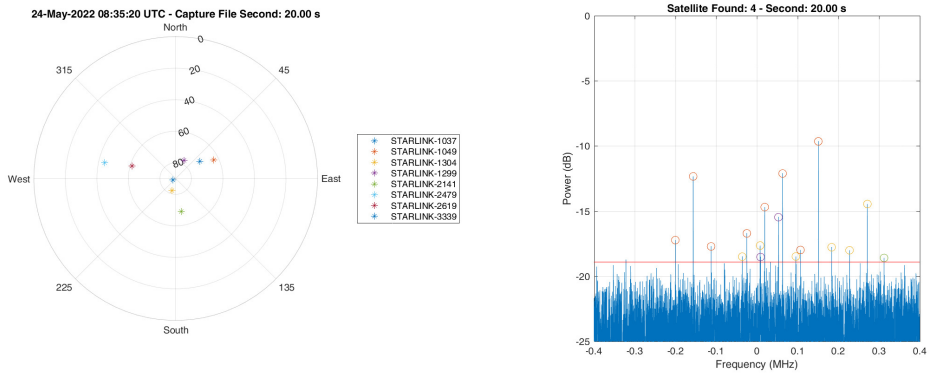

(b)

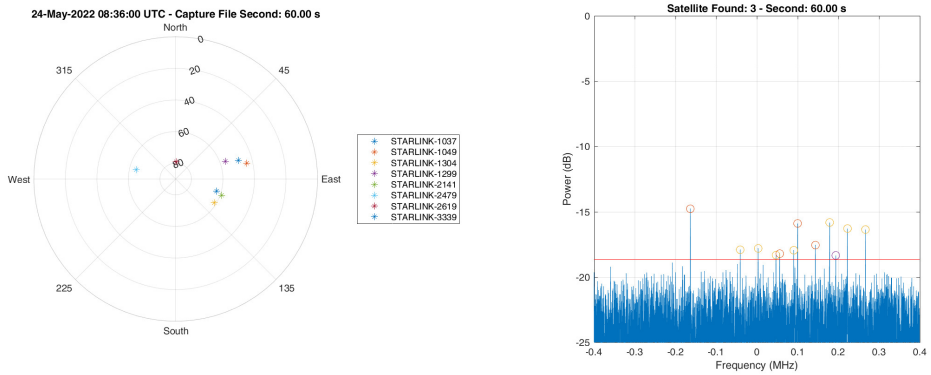

(c)

Figure 4.18: Comparison of Skyplot with corresponding peaks for (a) 0 seconds, (b) 20 seconds (c) 60 seconds

5 Discussion

This chapter discusses several aspects presented in the previous chapters, from the limitations imposed by the system inputs, such as acquisition files and TLEs, to the acquisition and tracking methods used. The importance of the visibility predictor is also clarified, illustrating a potential future application of the entire system designed and studied in this thesis. It also considers how this research can be extended to improve the quality of the acquired signal by improving the acquisition setup.

5.1 Capture File and Hardware Limitations

Files provided by ESA played a key role in the development of the tool for this thesis project. The use of real signals allowed the development of the necessary optimizations to address the specifics of the real LEO environment.

Although the first file used for the acquisition phase had many peaks and good SNR, the Doppler frequency shift noise present during the entire capture made it impractical to use for the tracking phase. In contrast, the second file used for tracking was not affected by the Doppler frequency shift noise, but the SNR was acceptable only for short intervals within the capture. This clearly demonstrated the importance of using a high-quality signal capture setup. The difference between the captures obtained using different hardware configurations emphasizes the significant impact that the choice of hardware can have on the quality of the captured signal.

The first acquisition was made with a basic configuration, using a KU-band LNB pointed at the zenith to record IQ data. Although an inexpensive LNB typical of commercial satellite TV was used, showing significant clock bias/drift and jitter due to the Local Oscillator (LO) quality, it still allowed clear detection of unmodulated tones. In contrast, the second capture was made with a higher quality LNB equipped with an external reference to minimize bias and clock jitter, ensuring a more stable and accurate signal. A possible reason for the poor quality of the second capture could be the limited coverage of the Starlink satellites at that specific location and time. No dish antenna was used in either capture, so the captures lost about 40 dB of gain. It should be noted that at least four satellites are required for accurate positioning during the entire capture, which is not verified in the capture files used. It is important to note, however, that despite these limitations, the files were useful in demonstrating the various blocks of the processing chain, even if independently.

In addition to the capture files, it is important to consider the limitations associated with TLEs and the SGP-4 model, such as the error of about 1 km per epoch, as mentioned in section 2.3.2, for any estimate provided by SGP-4, which can become a non-negligible error.

5.2 Future Software Improvements

After achieving an optimized setup and, consequently, a signal free of the problems illustrated in the previous section, it becomes possible to further continue the study introduced in this thesis.

In particular, as future improvements, during the tracking phase, the integration time T can be adjusted according to the scenario and the signal quality. For example, once the frequency lock is achieved, the integration time could be extended up to $T = 10$ ms to improve the SNR.

A further step consists of tracking all visible tones for a single satellite and then proceeding with the development of a system to aggregate these tones to obtain the best Doppler estimate for any given satellite.

With a signal that has good SNR over the entire capture, it will be possible to compare the Doppler profile with the Doppler estimates provided by the visibility predictor. In this way, the Satellite ID provided by the Visibility Predictor can be associated with the specific Doppler estimate.

5.3 GNSS Integration

In chapter 3, an assumption was made about knowing the receiver's position in order to filter satellites in the Visibility Predictor. This assumption, described in section 3.3.2, was made bearing in mind the possible future integration with a GNSS system. The Position, Velocity, Timing (PVT) provided by a GNSS system is essential for the Visibility Predictor to select only the relevant satellites. As a result, the system could support GNSS navigation by, for example, validating the MEO PVT in the case of spoofing attacks or providing position corrections in challenging scenarios. A diagram of the possible integration just described is shown in Figure 5.1. The scheme contains a new branch that includes the GNSS receiver and is integrated into the main system. The PVT determined by the GNSS is used to filter the satellites in the Visibility Predictor. This facilitates the identification of satellites by Doppler estimation in the tracking phase. In a subsequent step, the GNSS pseudoranges and Doppler measurements are fused with the Starlink system estimates to produce a more accurate PVT by combining data from both systems.

When considered for use in GNSS validation mode, such a system could operate in a snapshot mode. It should be noted, however, that the proposed integration is a complex challenge, requiring an advanced hardware infrastructure. This complexity is further increased by the fact that the front ends of the GNSS and LEO systems operate in different frequency bands.

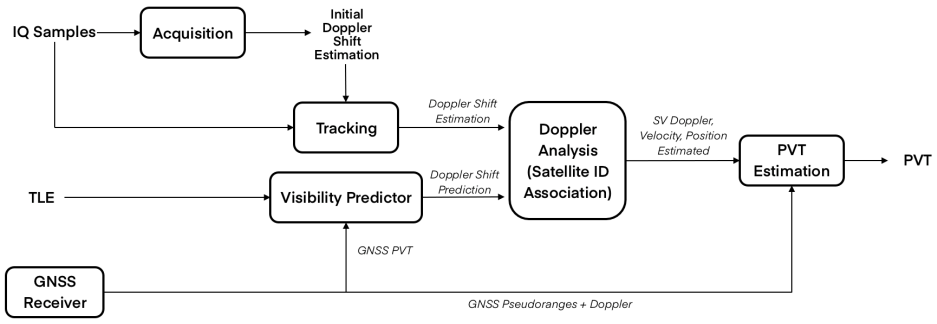

Figure 5.1: GNSS Integration Block Diagram

6 Conclusion

This chapter summarizes the results and the contents of this thesis. This work represents an evolution in the exploration of opportunistic navigation, with a focus on Starlink satellites due to their increasing prevalence in the current LEO satellite landscape. It then outlines prospects for future work, following the thoughts and discussions in Chapter 5.

6.1 Summary of Results

This thesis highlighted the potential of LEO orbit navigation systems. A review of the state of the art in chapter 2 has shown that it is possible to achieve accuracies on the order of tens of meters using only LEO orbiting satellites. This analysis is an important starting point for exploring the dynamics of the LEO environment and provides application insights for future dedicated LEO PNT systems that are expected to emerge in the near future.

Although several acquisition files were used during the course of this thesis, the central goal of developing acquisition, tracking, and visibility prediction modules was achieved effectively. As outlined in Chapter 5, the adoption of a more advanced acquisition setup could open up a more comprehensive analysis of the system and allow for an initial estimation of positioning using the Starlink satellites.

During the acquisition phase, signal processing and filtering techniques combined with the multi-threshold estimation approach proved their effectiveness in accurately identifying peaks.

In this context, the proper selection of the signal window and the estimation of the acquisition window length proved to be decisive in mitigating spectral leakage and ensuring optimal signal processing.

In the tracking phase, on the other hand, the configuration of the parameters is extremely important: the first exploration of the LEO environment revealed the strong dynamics of such systems. It is impressive to see how a tracking loop based on the use of FLL and PLL can not only reliably monitor a specific tone with a Doppler rate of 5 kHz, but also track values up to 14 kHz. This indicates that the system is far from reaching the dynamic limits typical of the LEO context, thus demonstrating the feasibility of a highly stable system.

The need to develop a visibility prediction tool was not arbitrary. A constellation such as Starlink, focused on Internet connectivity, does not provide signals specifically dedicated to navigation and therefore does not provide basic satellite status information such as position and velocity to the receiver. The implemented visibility prediction tool uses public TLE files released by NORAD. These, combined with the SGP-4 perturbation model, allow estimation of satellite position and velocity, effectively filling this gap in the system.

6.2 Future Work

The work presented in this thesis has paved the way for further developments in the field of opportunistic navigation using the Starlink satellites and other satellite systems in LEO orbit. The potential demonstrated suggests several areas of research and development that should be further explored:

- **Hardware and Software Improvements:** Both the hardware and the software developed play a key role in the quality of the captured signal and the success of the overall system. On the hardware side, implementing a capture system with higher sensitivity and accuracy could greatly improve the SNR. The use of higher quality LNBs, possibly combined with a parabolic antenna, could offer significant improvements in the quality of the captured signal, as discussed in 5.
  On the software side, there are several areas where the system can be refined:
  1. Optimization of the tracking phase: As mentioned earlier, during the tracking phase, adjusting the integration time T could improve the SNR. In addition, it may be beneficial to track all visible tones for a single satellite and aggregate this information to obtain a more accurate Doppler estimate.
  2. Satellite ID Identification: Once better signal acquisition is achieved, it may be possible to compare the Doppler profile with the Doppler estimates provided by

the Visibility Predictor, thus associating the satellite ID provided by the Visibility Predictor with the specific Doppler estimate.

3. Position Estimation: After optimizing the capture setup and refining the first phases of the system, such as acquisition, tracking and visibility prediction, the positioning phase can be developed. It is important to note that this phase requires the constant presence of at least 4 satellites in view.

These improvements, combined with deep analysis of the acquired data and close collaboration with experts in the field, could lead to significant innovations in the field of opportunistic navigation with LEO satellites.

- **Advanced Integration with GNSS:** One of the main conclusions of this thesis concerns the potential integration with GNSS systems. The assumption of a priori knowledge of the receiver position could be eliminated by directly integrating the proposed system with a GNSS module. This would allow the Visibility Predictor to operate in real time, using GNSS data to filter out relevant satellites and provide position corrections. Such integration would have the dual benefit of improving the accuracy of the GNSS system in challenging contexts and providing a backup system in case of GNSS failure or interruption.
- **Testing Under Real Conditions:** A natural evolution of this project could be to implement and evaluate the system in real-world conditions, conducting field tests to evaluate the performance of the system in different contexts, such as dense urban areas or remote regions.

In conclusion, this thesis has opened new frontiers in the research of opportunistic navigation with LEO satellites. The challenges and opportunities outlined suggest a promising future for this area of study, with many possible directions for further exploration and development.

References

[1] F. S. Prol, R. M. Ferre, Z. Saleem, P. Välisuo, C. Pinell, E. S. Lohan, M. Elsanhoury, M. Elmusrati, S. Islam, K. Çelikbilek, K. Selvan, J. Yliaho, K. Rutledge, A. Ojala, L. Ferranti, J. Praks, M. Z. H. Bhuiyan, S. Kaasalainen, and H. Kuusniemi, "Position, navigation, and timing (pnt) through low earth orbit (leo) satellites: A survey on current status, challenges, and opportunities," *IEEE Access*, vol. 10, pp. 83 971–84 002, 2022.

[2] J. Khalife, M. Neinavaie, and Z. M. Kassas, "The first carrier phase tracking and positioning results with starlink leo satellite signals," *IEEE Transactions on Aerospace and Electronic Systems*, vol. 58, no. 2, pp. 1487–1491, 2022.

[3] N. Jardak and R. Adam, "Practical use of starlink downlink tones for positioning," *Sensors*, vol. 23, no. 6, 2023. [Online]. Available: https://www.mdpi.com/1424-8220/23/6/3234

[4] Celestrak. Celestrak: Two-line element set format. [Accessed 23-August-2023]. [Online]. Available: https://celestrak.org/NORAD/documentation/tle-fmt.php

[5] ESA-Agency, "Leo pnt," 5 July 2022, [Accessed 23-August-2023]. [Online]. Available: https://www.esa.int/ESA_Multimedia/Images/2022/07/LEO_PNT

[6] Wikipedia, "Transit (satellite)," [Accessed 23-August-2023]. [Online]. Available: https://en.wikipedia.org/wiki/Transit_(satellite)

[7] R. Acharya, *Understanding Satellite Navigation*. Amsterdam: Academic Press, 2014.

[8] A. Cina, *Dal GPS al GNSS (global navigation satellite system): Per La Geomatica*. Celid, 2014.

[9] G. J.A Ávila Rodríguez, University FAF Munich, "Gnss modulation schemes," 2011, [Accessed 23-August-2023]. [Online]. Available: https://gssc.esa.int/navipedia/index.php/GNSS_Modulation_Schemes

[10] N. Jardak and Q. Jault, "The potential of leo satellite-based opportunistic navigation for high dynamic applications," *Sensors*, vol. 22, no. 7, 2022. [Online]. Available: https://www.mdpi.com/1424-8220/22/7/2541

[11] ESA-Agency, "New navigation missions for enhanced satnav and earth mapping," 6 July 2022, [Accessed 23-August-2023]. [Online]. Available: esa.int/Applications/Navigation/New_navigation_missions_for_enhanced_satnav_and_Earth_mapping

[12] ——, "International terrestrial reference frame," 5 July 2022, [Accessed 23-August-2023]. [Online]. Available: https://www.esa.int/ESA_Multimedia/Images/2022/07/International_Terrestrial_Reference_Frame

[13] L. Ries, M. C. Limon, F.-C. Grec, M. Anghileri, R. Prieto-Cerdeira, F. Abel, J. Miguez, J. V. Perello-Gisbert, S. D'Addio, R. Ioannidis, A. Ostillio, M. Rapisarda, R. Sarnadas, and P. Testani, "Leo-pnt for augmenting europe's space-based pnt capabilities," in *2023 IEEE/ION Position, Location and Navigation Symposium (PLANS)*, 2023, pp. 329–337.

[14] E.-M. Ahmed, W. Kan, , and A. Amir, "The potential of leo mega-constellations in aiding gnss to enable positioning in challenging environments (11396)," 11–15 September 2022, fIG Congress 2022 Volunteering for the future - Geospatial excellence for a better living Warsaw, Poland, 11–15 September 2022.

[15] T. G. Reid, B. Chan, A. Goel, K. Gunning, B. Manning, J. Martin, A. Neish, A. Perkins, and P. Tarantino, "Satellite navigation for the age of autonomy," *2020 IEEE/ION Position, Location and Navigation Symposium (PLANS)*, 2020.

[16] F. Farhangian and R. Landry, "Multi-constellation software-defined receiver for doppler positioning with leo satellites," *Sensors*, vol. 20, no. 20, 2020. [Online]. Available: https://www.mdpi.com/1424-8220/20/20/5866

[17] J. J. Khalife and Z. M. Kassas, "Receiver design for doppler positioning with leo satellites," in *ICASSP 2019 - 2019 IEEE International Conference on Acoustics, Speech and Signal Processing (ICASSP)*, 2019, pp. 5506–5510.

[18] M. L. Psiaki, "Navigation using carrier doppler shift from a leo constellation: Transit on steroids," *NAVIGATION*, vol. 68, no. 3, pp. 621–641, 2021. [Online]. Available: https://onlinelibrary.wiley.com/doi/abs/10.1002/navi.438

[19] Z. Kassas, J. Morales, and J. Khalife, "New-age satellite-based navigation–stan: simultaneous tracking and navigation with leo satellite signals," *Inside GNSS Magazine*, vol. 14, no. 4, 2019.

[20] Z. Tan, H. Qin, L. Cong, and C. Zhao, "Positioning using iridium satellite signals of opportunity in weak signal environment," *Electronics*, vol. 9, no. 1, 2020. [Online].

Available: https://www.mdpi.com/2079-9292/9/1/37

[21] H. Benzerrouk, A. Q. Nguyen, X. Fang, A. Amrhar, A. Nebylov, and R. J. Landry, "Alternative pnt based on iridium next leo satellites doppler/ins integrated navigation system," in *2019 26th Saint Petersburg International Conference on Integrated Navigation Systems (ICINS)*, 05 2019, pp. 1–10.

[22] S. Thompson, S. Martin, and D. Bevly, "Single differenced doppler positioning with low earth orbit signals of opportunity and angle of arrival estimation," 02 2021, pp. 497–509.

[23] T. E. Humphreys, P. A. Iannucci, Z. M. Komodromos, and A. M. Graff, "Signal structure of the starlink ku-band downlink," *IEEE Transactions on Aerospace and Electronic Systems*, pp. 1–16, 2023. [Online]. Available: https://doi.org/10.1109%2Ftaes.2023.3268610

[24] S. Aida and M. Kirschner, "Accuracy assessment of sgp4 orbit information conversion into osculating elements," 04 2013.

[25] Wikipedia, "Simplified perturbations models," [Accessed 23-August-2023]. [Online]. Available: https://en.wikipedia.org/wiki/Simplified_perturbations_models

[26] N. Instruments, "Understanding ffts and windowing," [Accessed 23-August-2023]. [Online]. Available: https://www.ni.com/en/shop/data-acquisition/measurement-fundamentals-main-page/analog-fundamentals/understanding-ffts-and-windowing.html

Acknowledgments

I would like to express my sincere gratitude to Professor Laurenti N., my supervisor, for his invaluable guidance and support throughout this academic journey. His expertise and dedication have been decisive in the completion of this thesis.

Furthermore, my appreciation extends to the entire Qascom team. In particular, I would like to highlight the importance of Elisa S., Fabio B., and Samuele F., whose collaboration and insights have been fundamental to my work.

My heartfelt thanks go to my family for their encouragement and support. I also wish to express deep gratitude to my girlfriend, Elisa V., who has been my point of reference for the entire time. Your understanding and patience during this challenging journey has been invaluable. Your ability to support, listen and guide me at critical moments really made a difference.

Finally, a heartfelt thank you to all of my friends who have been a constant source of inspiration and support and have made this journey unforgettable. Adelaide, Agata, Alejandro, Andrea B., Andrea M., Andrea O., Anna, Annachiara, Antonio, Arianna, Aurora, Carlotta, Cecilia, Clelia, Daniele, Davide, Elisa, Enrico D., Enrico T., Filippo, Francesco, Gabriele, Gaia, Giovanni, Giulia, Irene, Isabella, Isotta, Laura, Lucia, Marco, Maria Vittoria, Matteo P., Matteo T., Mirco, Riccardo L., Riccardo M., Sebastiano, Simone B., Simone T., Sofia C., Sofia T., Umberto, Virginia and others, thank you for the laughter, the support and the unforgettable moments.